ICESat-2 observations of blowing snow over Arctic sea ice during the 2019-2020 MOSAiC expedition

Joseph Robinson[1], Lyatt Jaeglé[1], Stephen P. Palm[2,3], Matthew D. Shupe[4,5], Glen E. Liston[6], Markus M. Frey[7]

[1] Department of Atmospheric and Climate Science, University of Washington, Seattle, WA, USA
[2] Science Systems and Applications, Lanham, MD, USA
[3] NASA Goddard Space Flight Center, Greenbelt, MD, USA
[4] Cooperative Institute for Research in Environmental Sciences, University of Colorado, Boulder, CO, USA
[5] National Oceanic and Atmospheric Administration, Physical Sciences Laboratory, Boulder, CO, USA
[6] Cooperative Institute for Research in the Atmosphere (CIRA), Colorado State University, Fort Collins, CO, USA
[7] Natural Environment Research Council, British Antarctic Survey, Cambridge, UK

Corresponding author: Joseph Robinson (jrobin15@uw.edu)

Key Points:

- Using an optimized algorithm, ICESat-2 derived blowing snow properties are consistent with observations from the MOSAiC drift
- ICESat-2 estimates of blowing snow sublimation at MOSAiC (2.38 cm SWE) match those inferred from the ground-based observations (2.56 cm SWE)
- Across the Central Arctic, ICESat-2 indicates blowing snow occurrence frequencies of 18-25%, with sublimation removing 16-17% of snowfall

Abstract

Blowing snow plays a key role in the surface mass and energy budgets of polar regions and can be a significant source of water vapor to the atmosphere. In this study, we optimize the algorithm for detecting blowing snow from NASA's Ice, Cloud and land Elevation Satellite 2 (ICESat-2) satellite for use over Arctic sea ice. We analyze six months (November 2019 through April 2020) of observations from the Multidisciplinary drifting Observatory for the Study of Arctic Climate (MOSAiC) campaign together with 612 nearly coincident (within 100 km) ICESat-2 overpasses to evaluate the ICESat-2 detection algorithm and inferred blowing snow properties. Both ICESat-2 and MOSAiC suggest a blowing snow occurrence frequency of 17% during the period of study. Blowing snow particle number and inferred from ICESat-2 show broad agreement with *in situ* observations made at 10 m above the surface during MOSAiC but are often well below observations made at 8 cm. Within a 100 km radius around the MOSAiC observatory, we find a cumulative blowing snow sublimation of 2.38 cm snow-water-equivalent (SWE), comparable to MOSAiC (2.56 cm SWE) and SnowModel-LG (2.35 cm SWE) estimates. This suggests that blowing snow sublimation removed 22-33% of snowfall during MOSAiC. Across the central Arctic, ICESat-2 and SnowModel-LG indicate blowing snow occurrence frequencies as high as 18-25%, with cumulative blowing snow sublimation fluxes (1.74-1.79 cm SWE) removing 16-17% of snowfall. These findings highlight the importance of blowing snow sublimation for the Arctic snow on sea ice budget.

Plain Language Summary

Blowing snow occurs when strong winds lift surface snow into the air. In polar regions, this process impacts the energy budget and results in snow loss through sublimation, thereby adding water vapor to the atmosphere. However, direct surface observations of blowing snow over Arctic sea ice are limited. Active satellite sensors, like the one on NASA's ICESat-2 satellite, help fill this gap by sending pulses of light toward the surface and measuring the signal returned. These high-resolution observations of blowing snow need to be validated against ground-based measurements. In this work, we combine ICESat-2 observations with surface measurements from an Arctic field campaign between November 2019 and April 2020. We first refine the methods used to detect blowing snow and estimate its properties using ICESat-2 and find these refinements align with the surface observations of blowing snow occurrence, particle number, and particle mass. Additionally, ICESat-2 estimates of blowing snow sublimation match the surface observations and predictions from a high-resolution computer simulation. Over the six-month period studied, the amount of snow lost to blowing snow sublimation accounts for 16-21% of total central Arctic snowfall, highlighting the significant role of blowing snow in the Arctic climate.

1 Introduction

Windblown snow plays a critical role in Earth's climate system, influencing a wide range of processes including sea and land ice mass balance (Déry & Yau, 2002; Gallée et al., 2001), the radiation budget of polar regions (Lesins et al., 2009; Y. Yang et al., 2014), polar tropospheric chemistry (Gong et al., 2023; Huang et al., 2020; Huang & Jaeglé, 2017; Krnavek et al., 2012; X. Yang et al., 2008), and the interpretation of physical and chemical ice core records (King et al.,

2004; Rhodes et al., 2017). Despite this marked importance, it is difficult to accurately describe the full spatial extent and temporal variability of blowing snow in polar regions. Long-term observations in both the Arctic and Antarctic are relatively scarce and often cover only specific regions or seasons (e.g., Déry & Yau, 2001; Mann et al., 2000; Nishimura & Nemoto, 2005).

Blowing snow sublimation is a significant removal path for snow and a source of moisture to the atmosphere. While some sublimation of snow occurs at the surface, it is greatly enhanced when snow particles are lofted into the atmospheric column, exposing their entire surface area (Liston & Sturm, 2004; Schmidt, 1982). Schmidt (1982) found that blowing snow sublimation can be up to two orders of magnitude greater than surface sublimation under similar conditions. J. Yang et al. (2010) report model estimates that blowing snow sublimation removes more than 27% of wintertime snowfall poleward of 70°N over Arctic sea ice. However, other studies (e.g., Chung et al., 2011) found a lower contribution of only 6% in their simulations, highlighting the large uncertainty in blowing snow model estimates. Accurately quantifying the impact of blowing snow sublimation on snow loss from the sea ice surface remains a key open area of research, particularly in a changing climate.

Over sea ice, blowing snow sublimation is also a source of sea salt aerosol (SSA; Frey et al., 2020; Ranjithkumar et al., 2025; Simpson et al., 2007; X. Yang et al., 2008, 2019) which play an important role in modulating polar atmospheric composition and climate. As snow accumulates on the sea ice, brine present at the ice/snow interface migrates into the snowpack (Geldsetzer et al., 2009; Perovich & Richter-Menge, 1994; Peterson et al., 2019). In addition, deposition of airborne SSA can introduce salt to the snowpack (Krnavek et al., 2012). Together, these processes result in the surface snow layer containing trace amounts of salt. When this salty snow is lofted into the atmosphere, its sublimation releases SSA, driving winter and spring SSA maxima observed in the Arctic and Antarctic (Huang and Jaeglé, 2017; Rhodes et al., 2017; X. Yang et al., 2019). Blowing snow SSA serves as a source of halogen species linked to ozone depletion events (Choi et al., 2018; Huang et al., 2020; Marelle et al., 2021; Swanson et al., 2022; Wales et al., 2023; X. Yang et al., 2010). Moreover, Gong et al. (2023) recently showed that blowing snow SSA enhances Arctic cloud condensation nuclei concentrations by up to an order of magnitude above background levels and induce during cloudy days a significant net surface warming of several watts per square meter through the alteration of cloud properties and lifetimes.

Several studies have attempted to create a more spatiotemporally complete record of blowing snow using models with varying levels of complexity. All of these approaches predict the onset of blowing snow based on meteorological parameters such as windspeed, temperature, snow age, or properties of the snow itself such as density (e.g., Gallée et al., 2001, 2013; Lenaerts et al., 2010, 2012, 2012). Gallée et al. (2013) used a regional climate model and compared blowing snow predictions to observations from two stations in Adélie Land, Antarctica. Their model was able to reproduce the overall frequency of blowing snow but underestimated the total observed flux of blowing snow during events in part due to a known bias in the acoustic measurement technique employed to detect blowing snow (Cierco et al., 2007; Naaim-Bouvet et al., 2010). Over boreal latitudes, development of models has focused largely on continents (e.g., Déry & Yau, 2001; Pomeroy et al., 1997), where blowing snow also negatively impacts populated areas. Additional studies expanded these approaches to sea ice regions (Chung et al., 2011; Déry &

Tremblay, 2004; Lecomte et al., 2015; Liston et al., 2018, 2020; J. Yang et al., 2010). However, the modeling approaches presented in these studies are based on empirical relationships of blowing snow processes derived from sparse observations, and there are no observationally-based constraints on these model calculations of pan-Arctic blowing snow over sea ice.

The use of spaceborne lidars can help fill observational gaps to examine the incidence and impacts of blowing snow over broad spatial and temporal scales. Palm et al. (2011, 2017, 2018) developed a blowing snow detection algorithm for the Cloud-Aerosol Lidar with Orthogonal Polarization (CALIOP) sensor aboard the NASA CALIPSO satellite (Winker et al., 2009). They showed that CALIOP lidar backscatter retrievals over Antarctica allow quantification of blowing snow properties, such as occurrence frequency, blowing snow height, optical depth, transport flux, and sublimation flux. A similar blowing snow detection algorithm (Palm et al., 2021; Herzfeld et al., 2021) was applied to the more recently launched NASA Ice, Cloud and land Elevation Satellite 2 (ICESat-2; Markus et al., 2017). The algorithms for both CALIOP and ICESat-2 were designed to detect and retrieve blowing snow properties over the Antarctic continent; however, Arctic sea ice is a substantially different environment where higher cloudiness relative to Antarctica (Zhang et al., 2019) and frequent low-level clouds, with bases below 1km altitude (Shupe et al., 2011), complicate the retrieval's ability to detect blowing snow.

In the present study, our goal is to optimize the ICESat-2 blowing snow retrieval algorithm over Arctic sea ice. We evaluate the optimized retrieval using six months (November 2019 through April 2020) of observations from the Multidisciplinary drifting Observatory for the Study of Arctic Climate (MOSAiC) expedition (Nicolaus et al., 2022; Rabe et al., 2022; Shupe et al., 2022). To estimate blowing snow transport and sublimation fluxes, we combine the optimized ICESat-2 retrieval algorithm with meteorological fields from reanalysis and particle size assumptions constrained by MOSAiC *in situ* observations. The inferred fluxes are evaluated against in situ MOSAiC observations and simulations from the state-of-the-art Lagrangian snow-evolution model SnowModel-LG (Liston et al., 2020).

In Section 2 we provide details on ICESat-2, MOSAiC, and SnowModel-LG. We also describe the modifications we applied to the ICESat-2 blowing snow algorithm to address challenges related to the high cloud occurrence over Arctic sea ice. In Section 3 we infer blowing snow occurrence frequency and properties using ICESat-2 and compare them to MOSAiC in situ observations and SnowModel-LG predictions for November 2019 through April 2020. We then examine blowing snow over the entire Arctic during the same period as observed by ICESat-2 and simulated with SnowModel-LG in Section 4, before providing concluding remarks in Section 5.

2 Datasets and Methods

2.1 Satellite blowing snow retrievals from ICESat-2

ICESat-2 was launched in 2018 to continue high resolution routine monitoring of the height of the Earth's surface, with emphasis on the change in ice sheet elevations. ICESat-2 is in a precessing orbit with an altitude of ~ 500 km and inclination of 92°, which allows for measurements up to 88° N latitude with a 91-day orbital repeat cycle (Markus et al., 2017). The

sole sensor aboard ICESat-2 is the Advanced Topographic Laser Altimeter System (ATLAS), which is a single wavelength (532 nm), high repetition rate (10 kHz) lidar system with photon counting detectors (Markus et al., 2017; Neumann et al., 2019). A diffractive optical element splits each laser pulse into 3 simultaneous beam pairs (one strong and one weak beam per pair) separated by about 3 km. Atmospheric backscatter is obtained by ATLAS using the three strong beams, spanning from the surface to an altitude of 14 km, with an along-track resolution of approximately 280 m and a vertical resolution of 30 m. To achieve this horizontal resolution, each 280 m ICESat-2 atmospheric profile represents the aggregate of 400 individual ATLAS laser shots (Palm et al., 2021). This study utilizes data from version 6 of the ATLAS/ICESat-2 Level 3A (ATL09) calibrated backscatter profile product (Palm et al., 2023). Only data from beam 1 are used in the analysis.

The algorithm for detecting blowing snow in the ATLAS backscatter profile is based on the CALIOP algorithm (Palm et al., 2011, 2018) and is described in Herzfeld et al. (2021) and Palm et al. (2021, 2022). In brief, in the presence of a detected surface return and 10 m windspeed > 4 m s^{-1} (from the NASA GEOS-5 FP-IT analysis) over snow covered land or sea ice, the blowing snow algorithm compares the atmospheric signal in the bin directly above the ground to the molecular (Rayleigh) scattering. If the atmospheric signal exceeds a fixed multiple of the molecular scattering, each successive vertical bin (moving upward) is interrogated until the backscatter falls below an adaptive threshold (about 2×10^{-5} m^{-1} sr^{-1}). The retrieved feature is required to touch the ground and not exceed 500 m in depth. If it passes both of these requirements, a blowing snow flag is assigned to the profile. Once blowing snow is retrieved, its vertical depth is logged and its optical depth (OD) is estimated as the sum of the backscatter within the blowing snow layer multiplied by the product of the bin depth (30 m) and the extinction to backscatter (lidar) ratio. A lidar ratio of 25 sr is used, which is a typical value for ice crystals in cirrus clouds (Chen et al., 2002; Josset et al., 2012).

We follow the work of Palm et al. (2017) and Déry & Yau (2002) to derive blowing snow particle number density, transport flux, and sublimation flux from the observed lidar backscatter. These calculations rely on meteorological fields from the NASA GEOS-5 FP-IT analysis (run at 0.5° latitude × 0.625° longitude; Lucchesi et al., 2015) and assumptions about blowing snow particle size, informed by MOSAiC observations. Further detailed descriptions are provided in Text S1.

2.2 Ground-based measurements during the MOSAiC expedition

The MOSAiC expedition began in September 2019 when the German research vessel Polarstern (Knust, 2017) was frozen into the sea ice north of the Laptev Sea. Observational platforms were housed onboard Polarstern and within ~ 2 km of Polarstern in a Central Observatory (Shupe et al., 2022). Two open-path snow particle counters (SPC; Nishimura et al., 2014; Nishimura & Nemoto, 2005) continuously measured the number and sizes of airborne snow particles in the diameter range 36–490 μm. These sensors were installed on the Met City meteorological tower as part of the Central Observatory, with an SPC at 8 cm (SPC_{8cm}) and the other at 10 m (SPC_{10m}) above the snow (Frey et al., 2023; Ranjithkumar et al., 2025). These heights were specifically chosen to help distinguish between falling and blowing snow (Shupe et al., 2022). The SPC measurements are combined with the windspeed observed at 2 and 10 m, respectively, to

calculate snow particle number density (m^{-3}) and snow-drift density (μ, kg m^{-3}). For the SPC at 8 cm, the observed 2 m windspeed is scaled to the measurement height assuming a logarithmic profile (Frey et al., 2020). Following the recommendation of Frey et al. (2020), we discard particle counts from the smallest and largest diameter class due to their larger uncertainty and increased influence from falling snow. Due to complications with installation, the SPC_{8cm} was only operational from 01 December 2019 onward. More detail on MOSAiC SPC observations can be found in Ranjithkumar et al. (2025).

Additional sensors installed on the Met City tower measured temperature, pressure, relative humidity (RH), and winds at nominal heights of 2, 6, and 10 m above the sea ice (Cox et al., 2023; Shupe et al., 2022). In addition, radiosondes were launched at least every 6 hours throughout the duration of MOSAiC. These sondes provided vertical profiles of temperature, RH, pressure, and winds from 12 m to 30 km. Jozef et al. (2023) developed a lower-atmospheric properties dataset built from the combination of MOSAiC radiosonde and ground-based observations, which includes the height and strength of temperature inversions as well as the presence, and base height, of boundary layer clouds. The cloud observations were provided by a Vaisala Ceilometer CL31 (ARM user facility, 2019) mounted on the deck of the Polarstern about 20 m above the ice surface. The ceilometer measured atmospheric backscatter at a wavelength of 910 nm with a temporal resolution of 16 s and a vertical resolution of 10 m. Beyond observing cloud properties, the ceilometer data were used as an independent check on the ICESat-2 retrieved blowing snow heights.

2.3 Blowing snow model simulations from SnowModel-LG

SnowModel-LG is a physics-based snow-on-sea ice model forced by atmospheric inputs of air temperature, RH, winds, and precipitation by the NASA Modern-Era Retrospective analysis for Research and Applications, version 2 (MERRA-2; Gelaro et al., 2017) as well as sea ice inputs of concentration and parcel motion (Tschudi et al., 2019, 2020). At each 3-hour timestep, SnowModel-LG performs mass-budget calculations where SWE depth evolution is accounted for by snow gains, losses, and sea ice dynamics (Liston et al., 2020).

The MERRA-2 fields used to force SnowModel-LG (0.5° latitude × 0.625° longitude) are first averaged from 1-hourly to 3-hourly and then distributed to the sea ice parcels using procedures in the MicroMet module (Liston & Elder, 2006). Moreover, SnowModel-LG is not forced directly by MERRA-2 snowfall but rather uses MERRA-2 water equivalent precipitation. MicroMet then defines the snowfall fraction of that water equivalent precipitation based on environmental conditions following Dai (2008). All MERRA-2 snowfall used in SnowModel-LG and quoted throughout this analysis have been bias corrected (as described in section 2.5 and Table 1 of Liston et al., 2020).

The SnowModel-LG blowing snow module, SnowTran-3D (Liston et al., 2007, 2018; Liston & Sturm, 1998) calculates the snow threshold friction velocity, u_{*t}, as a function of snow density, ρ_s, which is related to snow strength and hardness. The temporal evolution of ρ_s includes the histories of temperature, precipitation and wind-transport. The rate of blowing snow sublimation is a function of the vertical mass concentration distribution, temperature-dependent humidity gradients between the snow particles and the atmosphere, conductive and advective

energy- and moisture-transfer mechanisms, particle size, and solar radiation. SnowModel-LG blowing snow transport and sublimation fluxes are reported as column integrated values in units of kg m^{-1} s^{-1} and cm SWE d^{-1}, respectively.

Simulations of snow depth on Arctic sea ice from SnowModel-LG were evaluated against several independent datasets, including Operation IceBridge, ice mass balance buoys, and passive microwave estimates (Stroeve et al., 2020). With few exceptions, SnowModel-LG was shown to reproduce both the observed spatiotemporal variability of snow accumulation and depth ($r^2 > 0.70$) as well as significant reductions in snow depth over several Arctic sea ice regions in recent decades. Stroeve et al. (2020) did find agreement between SnowModel-LG and observations decreased in spring and summer due to overestimated melt in the model, but these periods largely lie outside of the cold season months (November through April) we analyze.

The version of SnowModel-LG used in this study is output as 3-hourly averages on a National Snow and Ice Data Center (NSIDC) Equal-Area Scalable Earth (EASE) grid (Brodzik & Knowles, 2002) with a resolution of 25 km.

2.4 Modifications to the ICESat-2 blowing snow detection algorithm

We modify the default ICESat-2 blowing snow algorithm to improve its ability to detect blowing snow over Arctic sea ice, particularly when clouds are present. The default algorithm faces two key challenges: 1) low Arctic clouds can be misidentified as blowing snow, and 2) thicker clouds attenuate the lidar signal below them, reducing the backscatter below the detection threshold and causing blowing snow to be mistakenly classified as clear air.

To address the misidentification of low clouds as blowing snow, we introduce two additional checks. First, if the height of maximum backscatter in the retrieved blowing snow feature exceeds 120 m, the retrieval is rejected and labeled as cloud. We chose this height because it is consistent with average ceilometer derived cloud base heights (146 m) during the MOSAiC campaign (Jozef et al., 2023; Section 2.2). Second, following Palm et al. (2017), we reclassify any blowing snow retrieval as cloud if the backscatter of any bin exceeds a threshold of 2.0×10^{-4} m^{-1} sr^{-1}, regardless of its altitude. We found that while exceptionally strong blowing snow can have observed backscatter which approaches this value, clouds almost always have bins which exceed 2.0×10^{-4} m^{-1} sr^{-1} (e.g., Figure S1-S2). The impact of these changes for an ICESat-2 overpass near MOSAiC is illustrated in Text S3 and Figure S1.

To correct for the attenuation due to transmissive clouds, we introduce a scaling factor that adjusts the near-surface backscatter based on the ratio of the apparent surface reflectance (ASR) to the true surface reflectance (SR). This ratio is a measure of the two-way atmospheric transmission (T^2) and thus an indicator of the presence and optical depth of clouds (Palm et al., 2022; Y. Yang et al., 2013). True SR values are derived from a monthly average of clear-sky (no detected cloud or aerosol layers) ICESat-2 measurements between 2018-2021 (Palm ext al., 2022). The scaling factor we apply is $1/T^2$ (= SR / ASR). We apply this scaling factor to the lowest 120 m of the backscatter profile before running the blowing snow algorithm. For ICESat-2 observations near the MOSAiC observatory, the median SR was 0.60 (interquartile range of 0.59-0.61; Figure S3a), while the median ASR for profiles with a detected surface was 0.29

(interquartile range of 0.08-0.48; Figure S3b). The resulting median SR / ASR scaling factor was 2.05 (interquartile range of 1.25-7.23; Figure S3c). The effect of this scaling is illustrated in Text S4 and Figures S2 for an ICESat-2 overpass near MOSAiC.

We examined the overall effect of introducing these modifications by conducting a sensitivity test across the entire Arctic during February 2020. This test compared the default algorithm (no reclassification of retrievals as cloud and no scaling for cloud attenuation) to scenarios with one or both modifications turned on. Overall, we found that our first modification reclassifies 14 % of retrievals as cloud, while our second enhances the blowing snow occurrence frequency from 15 % (using the default algorithm) to 22 %.

A final modification we implement is to consider the attenuation of the lidar signal as it propagates through the blowing snow feature. This attenuation can lead to an underestimation of the backscatter, which in turn affects the derived blowing snow transport and sublimation fluxes near the surface. We correct this attenuation by cumulatively integrating the extinction, starting at the top bin of blowing snow and working downwards towards the surface. In doing so, we also account for the two-way transmission between each bin and the top of the blowing snow feature. While only applied to Arctic sea ice in this study, the modifications we describe could have applicability for differentiating near-surface scattering layers and clouds in other regions.

2.5 Identification and classification of ICESat-2 coincidences with MOSAiC

We define ICESat-2 orbits as coincident with the MOSAiC observatory if the beam ground-track passed within 100 km of the drift location. By varying this distance criterium, we found that the 100 km search radius balances maximizing the number of coincidences with ensuring similar air mass sampling by ICESat-2 and MOSAiC.

We then assign each of the coincident ICESat-2 overpasses one of four categories: blowing snow, mixed, clear air, or cloudy/attenuated. These categories are based on the distribution of ICESat-2 profile types within each coincidence. If more than 70% of all profiles are attenuated due to cloud (i.e., the surface cannot be detected), the coincidence is labeled as cloudy/attenuated. We assign the other three categories based on the occurrence frequency of blowing snow in the non-attenuated profiles. We label the coincidences as blowing snow if more than 50% of profiles are blowing snow, mixed if 15-50% of profiles are blowing snow, and clear air if less than 15% of profiles are blowing snow.

3 Results

3.1 Coincidence of ICESat-2 orbits with the MOSAiC drift

The November 2019 through April 2020 period encompassed the first three of five MOSAiC expedition legs, during which the observatory drifted across the central Arctic Ocean (Figure 1a). Except for a two-week period from late February to early March 2020, the observatory remained south of 88^{o} N, the highest latitude observable by ICESat-2 (red circle, Figure 1a). With the coincidence definition described in section 2.5, we identify 612 ICESat-2 orbits coincident with MOSAiC (Figure 1b). The number of monthly coincidences increased from 64 in November, peaked at 164 in January, and decreased to 46 in April as MOSAiC quickly drifted southward

(Figure 1b). These coincidences encompassed 346,820 individual ICESat-2 profiles, with on average 566 ICESat-2 profiles within 100 km of MOSAiC per coincident overpass (Figure 1c). The number of coincident overpasses on any given day was typically 3-5 (Figure 1d), with up to 6 coincidences on several days in January, February, and March as MOSAiC drifted near 88° N.

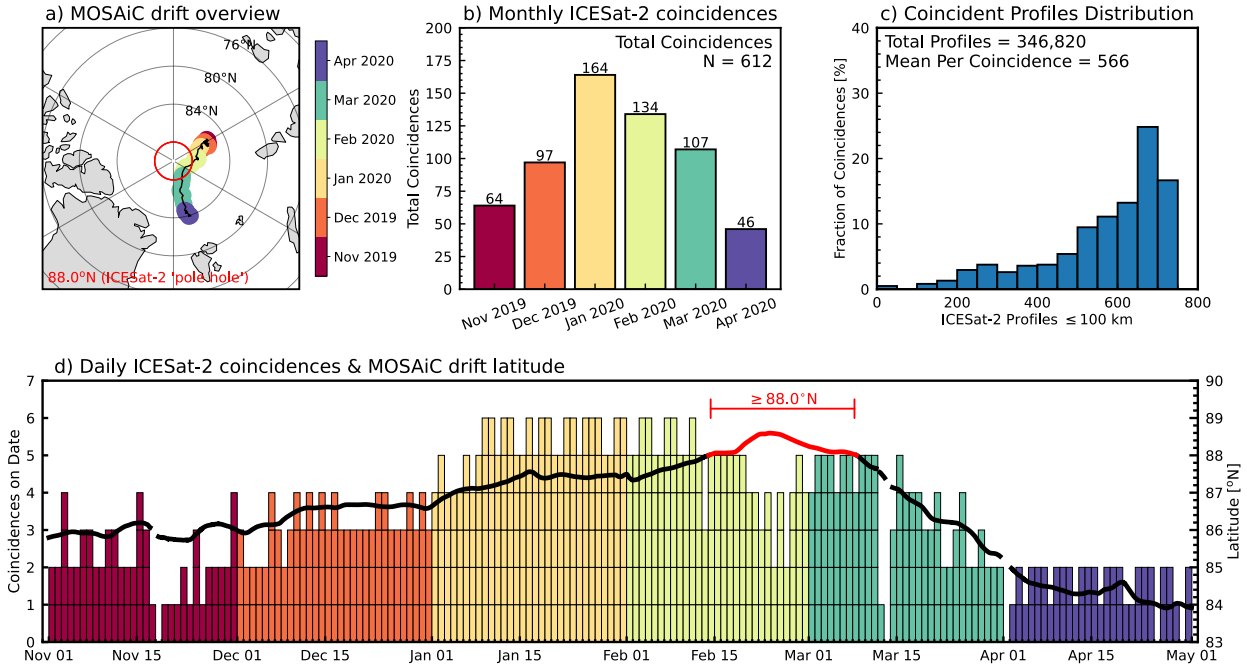

Figure 1. Overview of the MOSAiC drift and ICESat-2 coincidences for November 2019 through April 2020. **(a)** Track of the MOSAiC drift (black line) with the drift month displayed as colors. At each point, the shaded area represents a circle with a radius of 100 km centered on the drift. The red circle represents the poleward extent of ICESat-2 orbits (88° N). **(b)** Monthly number of ICESat-2 overpasses coincident with MOSAiC. **(c)** Distribution showing the number of ICESat-2 profiles within 100 km of the MOSAiC drift per coincident overpass. The total number of profiles and the mean number of profiles per coincidence are shown in the legend. **(d)** Daily timeseries of the number of ICESat-2 coincident overpasses colored by month. Multiple coincidences on a given day are shown as stacked bars. The MOSAiC drift latitude is indicated as a black line, with the period when it was poleward of 88° N highlighted in red.

Figures 2a and 2b show the hourly timeseries of 10 m windspeed (U_{10m}) and snow-drift density at 8 cm (μ_{8cm}) observed during MOSAiC. We identify MOSAiC blowing snow events using the following three criteria: 1) U_{10m} exceeds 5 m s^{-1}; 2) μ_{8cm} exceeds 1×10^{-5} kg m^{-3}; and 3) the snow-drift density at 10 m (μ_{10m}) exceeds 1×10^{-7} kg m^{-3}. Since the 8 cm SPC data were unavailable in November 2019, only the U_{10m} and μ_{10m} criteria are applied for that period. These criteria differ slightly from the blowing snow event identification of Gong et al. (2023), who used the same μ_{8cm} threshold, but set a higher U_{10m} threshold based on the Li & Pomeroy (1997) empirical model (which is a function of temperature, and is ~ 7 m s^{-1} on average). We chose instead a fixed blowing snow threshold windspeed of 5 m s^{-1} near the lower end of available MOSAiC observations (see Figure 8 of Ranjithkumar et al. 2025). Our additional μ_{10m} threshold helps exclude periods of shallower, drifting snow that ICESat-2 is less likely to detect. By applying our criteria to the MOSAiC observations, we identify 724 hours as blowing snow, across 27 individual events (gray shading, Figure 2), resulting in an hourly blowing snow occurrence frequency of 17%. This is slightly lower than Gong et al. (2023), who reported a 20% frequency

without the μ_{10m} threshold. However, the number and timing of the events remains consistent across both methods.

During blowing snow periods, μ_{8cm} reached values as high as 1×10^{-2} kg m^{-3} (Figure 2b), with μ_{10m} (not shown) maximizing about one order of magnitude lower at 1×10^{-3} kg m^{-3}. Figure 2b also shows the daily SnowModel-LG blowing snow transport flux (green line, Figure 2b), obtained by averaging the model 25 km grid cells within 100 km of MOSAiC (about 48-50 grid cells per day). We find that SnowModel-LG generally reproduces the timing of blowing snow events, particularly in February and March.

Figure 2c shows the 612 ICESat-2 coincidences color-coded according to their classification (Section 2.5): blowing snow (magenta), mixed (mixture of blowing snow profiles and clear air, green), clear air (orange), or cloudy/attenuated (blue). Of the 540 non-cloudy coincidences, 92 are classified as blowing snow, resulting in an 17% occurrence frequency, in agreement with the 17% occurrence frequency found from the MOSAiC observed snow-drift density and windspeed.

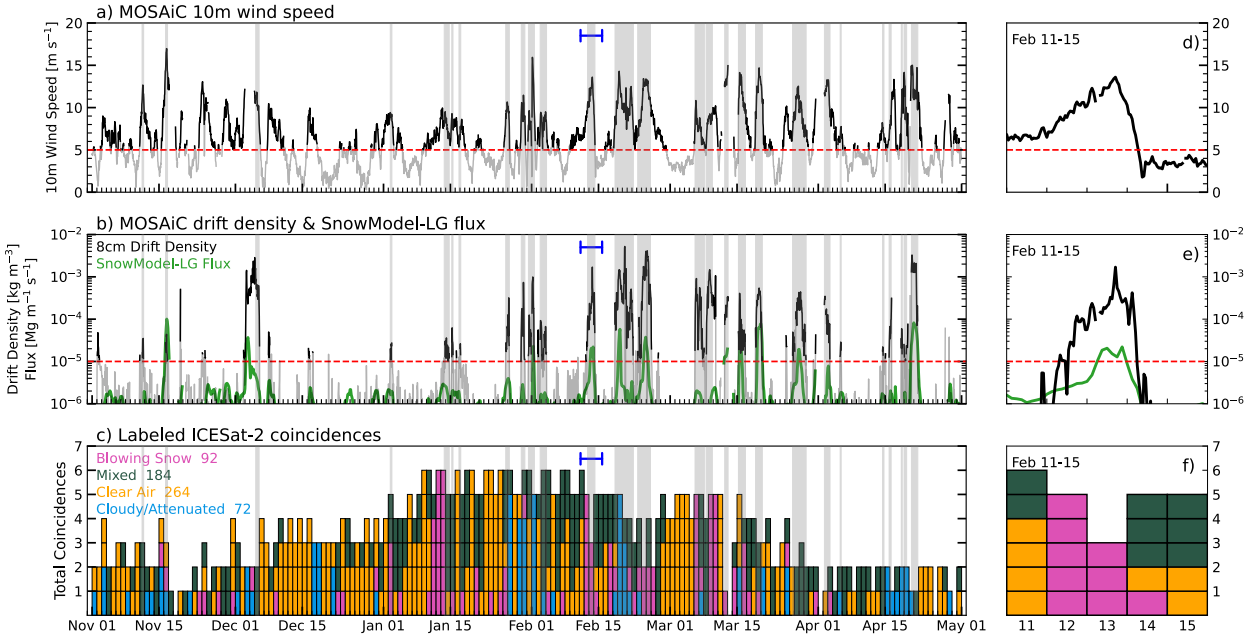

Figure 2. (a) Hourly timeseries of MOSAiC observed 10m windspeed (black line, units m s^{-1}), with the 5 m s^{-1} threshold for blowing snow shown as a dashed red line. **(b)** Hourly timeseries of MOSAiC snow-drift density at 8cm (μ_{8cm}, black line, units kg m^{-3}), with the 10^{-5} kg m^{-3} snow-drift threshold indicated in red. The 3-hourly timeseries of SnowModel-LG column integrated blowing snow mass transport flux is also shown (green line, units Mg m^{-1} s^{-1}). **(c)** ICESat-2 coincident overpasses classified as blowing snow (magenta), mixed (green), clear air (orange), or cloudy/attenuated (blue) as described in Section 2.5. For all panels, the vertical gray shading indicates periods identified as blowing snow in the MOSAiC data. The 11-15 February 2020 blowing snow storm is marked by a dark blue bracket in each panel. **(d-f)** As in (a-c) but for the period of 11-15 February 2020.

Several intense blowing snow periods during MOSAiC were due to major storms, especially in late February and mid-April (Rinke et al., 2021; Shupe et al., 2022), and were not observable by ICESat-2 due to cloudy conditions. However, at other times, such as mid-February and the second week of March, ICESat-2's blowing snow classification aligns well with the MOSAiC observations of blowing snow. Notably, from 11 to 15 February, ICESat-2 captured the full

progression of a 3-day blowing snow event observed by MOSAiC (Figure 2d-f). During this period, ICESat-2 initially observed clear air for four coincidences on 11 February, then detected blowing snow coincidences between 12 and 14 February, corresponding with strong increases in U_{10m}, μ_{8cm}, and SnowModel-LG blowing snow flux. By late 14 February into 15 February, no ICESat-2 coincidences were observed as blowing snow. This period is analyzed more closely in the following section (a second case study for 8-11 March is presented in the Supporting Information, text S6 and Figure S5).

3.2 11-13 February 2020 case study of blowing snow

Figure 3 shows three ICESat-2 coincident backscatter curtains encompassing the onset and maintenance of the 11-13 February blowing snow event. On 11 February ICESat-2 detected a clear return from the surface and no atmospheric scattering within 100 km of MOSAiC (Figure 3a). There was some blowing snow retrieved by ICESat-2, but it occurred more than 120 km from MOSAiC (right side, Figure 3a) and was comparatively weak (OD = 0.04). At the same time, observations at Met City recorded moderate winds (U_{10m} = 6.5 m s^{-1}; Figure 2d), with negligible snow-drift (μ_{8cm} = 9.8×10^{-11} kg m^{-3}; Figure 2e), and no snow particles observed at 10 m. In addition, the coincident radiosonde launch identified a very shallow surface inversion (height = 50 m, Figure 3b) and the ceilometer mounted on the Polarstern detected no backscatter (Figure S4a).

On 12 February, ICESat-2 detected blowing snow across the entire coincident overpass, with over 90% of profiles within 100 km of MOSAiC classified as blowing snow (Figure 3c). Ground observations from MOSAiC indicated the onset of blowing snow around this time, with U_{10m} increasing to 8.8 m s^{-1} and μ_{8cm} to 1.2×10^{-5} kg m^{-3} (Figure 2d-e). The mean height of the blowing snow observed by ICESat-2 was 97 m, consistent with the depth of the surface temperature inversion identified in the coincident radiosonde launch (100 m, Figure 3d). Moreover, the ceilometer also observed elevated backscatter in the lowest 100 m coincident with this overpass, with a mean top of the feature at 110 m (Figure S4b).

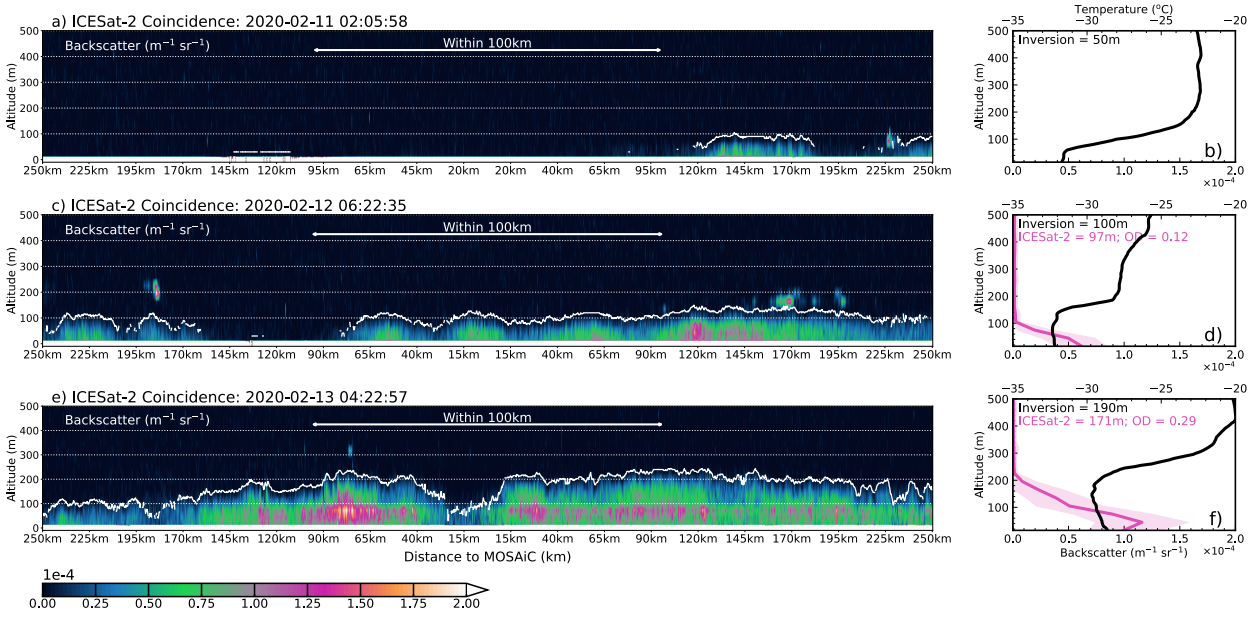

Figure 3. ICESat-2 overpasses coincident with MOSAiC observations during the 11-13 February blowing snow storm. **Left column:** Curtains of ICESat-2 calibrated, attenuated backscatter between the surface and 500m (shading, units m^{-1} sr^{-1}). The x-axis indicates the distance from the MOSAiC observatory (in km). The thick white line in each curtain plot represents the top of ICESat-2 retrieved blowing snow. **Right column:** Vertical profiles of ICESat-2 calibrated, attenuated backscatter averaged within 100 km of the MOSAiC drift (magenta line, with shading corresponding to ± 1 standard deviation). MOSAiC radiosonde profiles of temperature (black line) for the launch closest in time to each ICESat-2 overpass are also shown. The legend indicates the height of the temperature inversion identified in the radiosonde temperature profile, as well as the average height and optical depth of ICESat-2 blowing snow retrievals within 100 km of the MOSAiC drift.

Both MOSAiC and ICESat-2 observations indicate strengthening of the blowing snow event on 13 February (Figure 3e,f). At the surface, U_{10m} approached 12 m s^{-1} (Figure 2d), with significant snow-drift density observed at both 8 cm (μ_{8cm} = 1.5×10^{-3} kg m^{-3}; Figure 2e) and 10 m (μ_{10m} = 3.5×10^{-7} kg m^{-3}). ICESat-2 retrievals show that the blowing snow layer had deepened, with a mean height of 171 m near MOSAiC, and intensified (mean OD = 0.29). The strengthening of the blowing snow was also observed by the ground-based ceilometer, which observed a stronger backscatter signal reaching deeper heights (mean 174 m, Figure S4c). Temperature below 200 m had increased by 5°C, and the temperature inversion had deepened to 190 m, indicative of stronger mixing in the lowest levels of the atmosphere (Figure 3f). Taken together, the 12-13 February ICESat-2 overpasses suggest that during blowing events lofted particles often reach the top of the capping inversion, consistent with the Antarctic case studies presented in Palm et al. (2018).

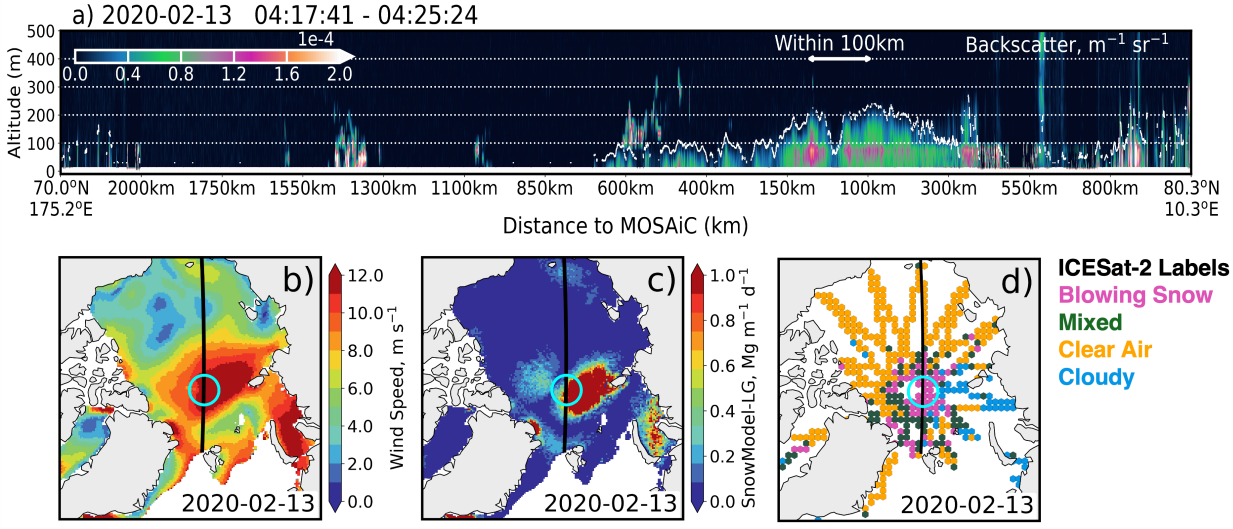

Figure 4. Expanded view of the 13 February 2020 blowing snow event. **(a)** Curtain of ICESat-2 calibrated, attenuated backscatter between the surface and 500 m (shading, units m^{-1} sr^{-1}) for all profiles over sea ice. This orbit corresponds to the segment highlighted in Figure 3e, with the portion within 100 km of the MOSAiC observatory indicated by the white arrow. Spatial distribution of **(b)** 10 m MERRA-2 windspeed (units m s^{-1}), **(c)** SnowModel-LG predicted blowing snow transport flux (shading, units Mg m^{-1} d^{-1}), and **(d)** classifications based on ICESat-2 observations, using a 100 km grid spacing. Grid cells in (d) are classified using the approach described in Section 2.5: blowing snow (magenta), mixed (green), clear air (orange), or cloudy/attenuated (blue). In panels b-d, black lines correspond to the ICESat-2 orbit shown in (a) and cyan circles are centered on MOSAiC and have a radius of 250 km.

Figure 4 illustrates the full horizontal extent of blowing snow on 13 February as observed by ICESat-2, with near continuous detections spanning over 1,000 km along track (Figure 4a). In the region near MOSAiC (cyan circles), MERRA-2 windspeeds were > 10 m s^{-1} (Figure 4b), with SnowModel-LG predicting significant blowing snow mass transport (> 0.80 Mg m^{-1} d^{-1}, Figure 4c) aligned with the ICESat-2 detections (magenta points, Figure 4d). On this day, both ICESat-2 and SnowModel-LG suggest blowing snow occurred across an area of about 1.5 million km^2, comparable in size to the state of Alaska. Taken together, Figures 3 and 4 illustrate the large spatial footprint of this event and underscore its synoptic-scale nature.

3.3 Blowing snow heights, number concentrations, and mass concentrations from ICESat-2 and MOSAiC

Do retrieved ICESat-2 blowing snow depths always coincide with identified temperature inversion heights? What factors control the retrieved blowing snow depth? To answer these questions, we broaden our examination to 253 ICESat-2 coincident overpasses categorized as either blowing snow (n = 83) or mixed (n = 170) paired with MOSAiC sonde launches within 6 hours of each overpass.

Figure 5a shows that inversion heights for this subset of radiosonde profiles peak broadly between 25 and 175 m, with a mean of 109 m. For comparison, the mean observed inversion height over the entire November through April period is 156 m. ICESat-2 blowing snow retrievals in this subset of coincidences show a mean height of 86 m, maximizing between 60 and 120 m. Most retrieved blowing snow heights fall at or just below the inversion layer, displaying a moderately strong correlation (r = 0.67) with the radiosonde inversion height (Figure 5b).

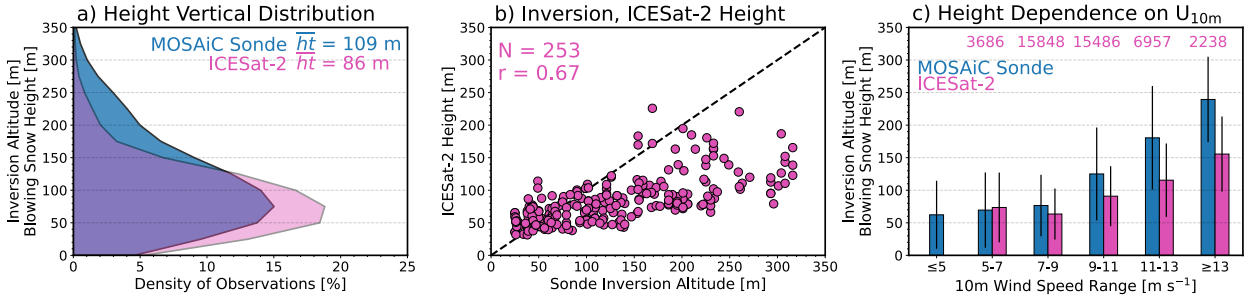

Figure 5. (a) Distribution of inversion altitudes from MOSAiC radiosonde launches (blue) and blowing snow heights from ICESat-2 (magenta) in coincidences classified as blowing snow or mixed. The legend includes the mean height for each. **(b)** Correlation between radiosonde inversion altitude and mean ICESat-2 blowing snow height. **(c)** Dependence of inversion heights (blue) and ICESat-2 blowing snow heights (magenta) with 10m windspeed. Bar heights represent the average and error bars are ± 1 standard deviation. The observations are grouped into 2 m s^{-1} windspeed bins between 5-13 m s^{-1}. All observations occurring at windspeeds ≥ 13 m s^{-1} are grouped into the final bin. Also shown is the average and standard deviation of inversion heights for all launches occurring at windspeeds < 5 m s^{-1}. The numbers at the top of the panel indicate the number of ICESat-2 blowing snow profiles in each windspeed bin.

Both the radiosonde observations and ICESat-2 suggest U_{10m} controls much of the observed variability in inversion and blowing snow heights (Figure 5c), consistent with deeper vertical mixing during periods of stronger winds (Jozef et al., 2024; Sterk et al., 2013). The inversion

heights increase from 50 m to nearly 200 m as U_{10m} increases from 5 m s^{-1} to more than 11 m s^{-1}. Over the same range, ICESat-2 retrieved blowing snow heights increase by a factor of 3 from 50 m to 150 m on average.

We now turn our focus to blowing snow properties inferred from ICESat-2 and compare them to MOSAiC and SnowModel-LG. Figure 6 shows the snow particle number densities and mass concentrations inferred from ICESat-2 backscatter during the 13 February blowing snow event (same overpass as in Figure 3e). The derivation of these blowing snow properties from the retrieved backscatter depends on assumptions about the lidar ratio and snow particle size profile (Supporting Information, Text S1-S2). Significant snow particle number densities (2.5-5.0×10^5 m^{-3}) are inferred from ICESat-2, with maxima close to the MOSAiC drift occurring 30-100 m off the surface (Figure 6a). Despite backscatter being maximum at the surface (Figure 3f), the assumed decrease in particle size with height (Text S2) results in particle numbers maximizing above the surface. Inferred particle mass concentrations decrease by a factor of 6 from the surface (> 0.60×10^{-4} kg m^{-3}) to the top of the blowing snow layer (< 0.10×10^{-4} kg m^{-3}; Figure 6b). Figures 6c and 6d compare the mean and range of ICESat-2 snow particle number densities and mass concentrations in the lowest atmospheric bin, centered at 15 m, to the MOSAiC SPC observations, averaged within 6 hours of the overpass. The ICESat-2 mean number density (1.46×10^5 m^{-3}) and mass concentration (3.62×10^{-5} kg m^{-3}) compare well with the SPC observations at 10 m (2.28×10^5 m^{-3} and 5.51×10^{-5} kg m^{-3}) but, as expected, are lower than the SPC observations at 8 cm.

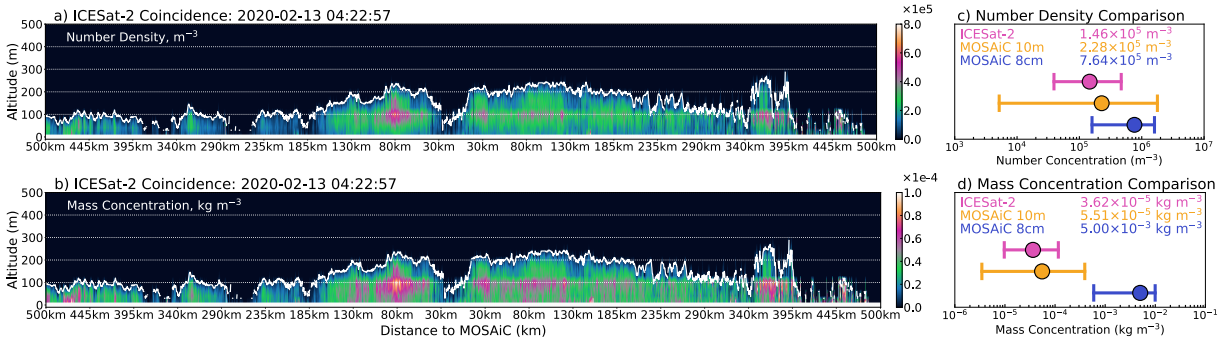

Figure 6. ICESat-2 inferred snow particle number density (top row) and mass concentration (bottom row) for a coincidence on 13 February 2020. **(a,b)** Curtain plot of ICESat-2 blowing snow number density (units m^{-3}, panel a) and mass concentration (units kg m^{-3}, panel b). The thick white line in each panel represents the top of ICESat-2 retrieved blowing snow layers. **(c,d)** Comparison of mean blowing snow particle number density and mass concentrations from ICESat-2 and MOSAiC observations. ICESat-2 values (magenta) are derived from the lowest atmospheric bin (centered at 15 m) within 100 km of the MOSAiC drift. MOSAiC in situ measurements at 8 cm (blue) and 10 m (orange) are averaged within 6 hours of the ICESat-2 overpass. Circles indicate the mean values and error bars represent the observed range (minimum to maximum).

Figure 7 evaluates more systematically the ICESat-2 derived snow particle number densities and mass concentrations against MOSAiC observations during 217 blowing snow and mixed coincidences. MOSAiC snow particle number densities at 8 cm showed a median value of 1.72×10^5 m^{-3} (Figure 7a), an order of magnitude larger than observed at 10 m (median 2.45×10^4 m^{-3}). The number densities inferred from ICESat-2 in the lowest atmospheric bin display median values of 1.10×10^5 m^{-3} (Figure 7a) and range from 3.58×10^4 – 4.90×10^5 m^{-3}. The range of observable number densities is limited by the lower and upper bounds of backscatter assumed in

the blowing snow retrieval (1-2×10^{-5} – 2×10^{-4} m^{-1} sr^{-1}). The number density distributions further indicate that ICESat-2 displays better agreement with the SPC_{10m} observations compared to SPC_{8cm}, with a lower mean absolute error (MAE) (2.04×10^{5} m^{-3} compared to 5.59×10^{5} m^{-3}) and a reduced MOSAiC to ICESat-2 bias (-2.81×10^{4} m^{-3} compared to +4.48×10^{5} m^{-3}).

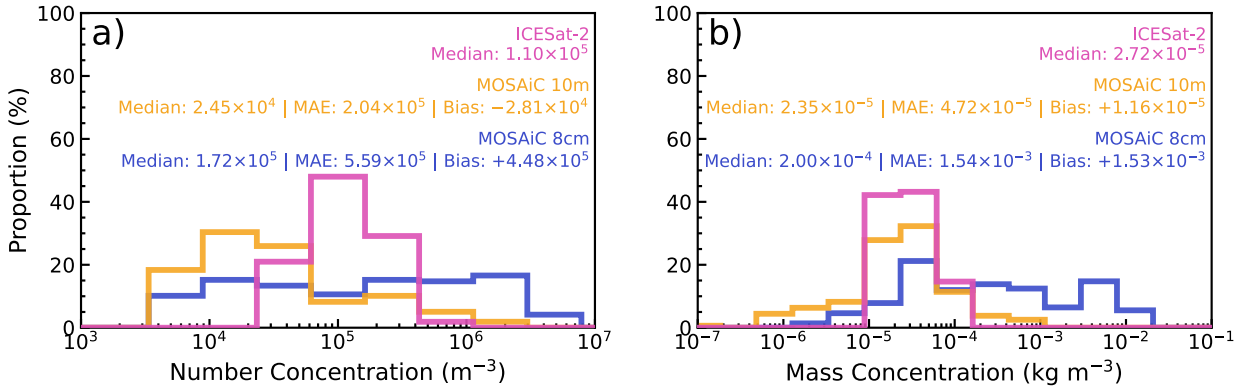

Figure 7. Distributions of **(a)** blowing snow particle number densities and **(b)** mass concentrations observed during MOSAiC and inferred from ICESat-2. The ICESat-2 distributions (magenta) are pooled for coincidences classified as blowing snow or mixed and represent the average inferred from the lowest atmospheric bin for blowing snow retrievals within 100 km of MOSAiC. The distributions from the MOSAiC SPC sensors at 8 cm (blue) and 10 m (orange) are from observations occurring within 6 hours of each ICESat-2 coincidence. The mean absolute error (MAE) and bias of the MOSAiC observations relative to ICESat-2 are shown in the legends.

Observed SPC_{8cm} particle mass concentrations (median 2×10^{-4} kg m^{-3}; Figure 7b) are again an order of magnitude larger than SPC_{10m} (median 2.35×10^{-5} kg m^{-3}). The ICESat-2 inferred values (median 2.72×10^{-5} kg m^{-3}; Figure 7b) align more closely with the SPC_{10m} observations, with a lower MAE (5.42×10^{-5} kg m^{-3}) and bias (+1.16×10^{-5} kg m^{-3}) compared to the SPC_{8cm} observations (MAE: 1.60×10^{-3} kg m^{-3}, bias: +1.53×10^{-3} kg m^{-3}). We thus find that ICESat-2 derived number and mass concentrations are comparable to *in situ* measurements taken at 10 m above the surface. Moreover, the reasonable agreement in particle number and mass across ICESat-2 coincidences lends confidence to the estimates of blowing snow transport and sublimation fluxes, which we examine next.

3.4 Blowing snow transport and sublimation fluxes from ICESat-2, MOSAiC, and SnowModel-LG

Figure 8 shows the daily timeseries of blowing snow transport and sublimation fluxes derived from ICESat-2, MOSAiC, and SnowModel-LG along the MOSAiC drift. The ICESat-2 fluxes are averaged over all blowing snow detections within a 100 km radius of MOSAiC, weighted by the occurrence frequency of blowing snow. Similarly, we average daily SnowModel-LG results within 100 km of MOSAiC and ignore grid cells which ICESat-2 observes as cloudy. We estimate daily blowing snow transport and sublimation fluxes from hourly MOSAiC SPC_{8cm} and Met City observations following Déry & Yau (1999, 2001, 2002), with details in Text S5.

The daily timeseries of blowing snow transport shows marked periods of intense transport (> 2 Mg m^{-1} d^{-1}) coinciding with periods of blowing snow identified in the MOSAiC data (gray inserts, Figure 8a). All three estimates show correlation with each other (r = 0.43-0.73) as the

main driver for transport flux is windspeed. Inferred ICESat-2 column integrated transport fluxes (mean 0.53 Mg m^{-1} d^{-1}) are nearly a factor of three larger than SnowModel-LG (mean 0.19 Mg m^{-1} d^{-1}). While both values represent a column integrated transport, the difference can be explained by SnowModel-LG largely confining the blowing snow to the lowest several meters of the atmosphere. Meanwhile, ICESat-2 observes blowing snow extending to deeper heights (Figure 3-5) where windspeeds tend to be faster (Figure S6b). The transport flux within the saltation layer, derived from the SPC_{8cm} observations, has a lower mean value of 0.12 Mg m^{-1} d^{-1}. The fact that the ICESat-2 estimate exceeds this value by a factor of four suggests that a substantial fraction of the total blowing snow transport occurs above the saltation layer. This is consistent with Liston & Sturm (1998), who showed that for windspeeds > 9 m s^{-1}, the magnitude of blowing snow transport in the lofted blowing snow layer exceeds that in the saltation layer.

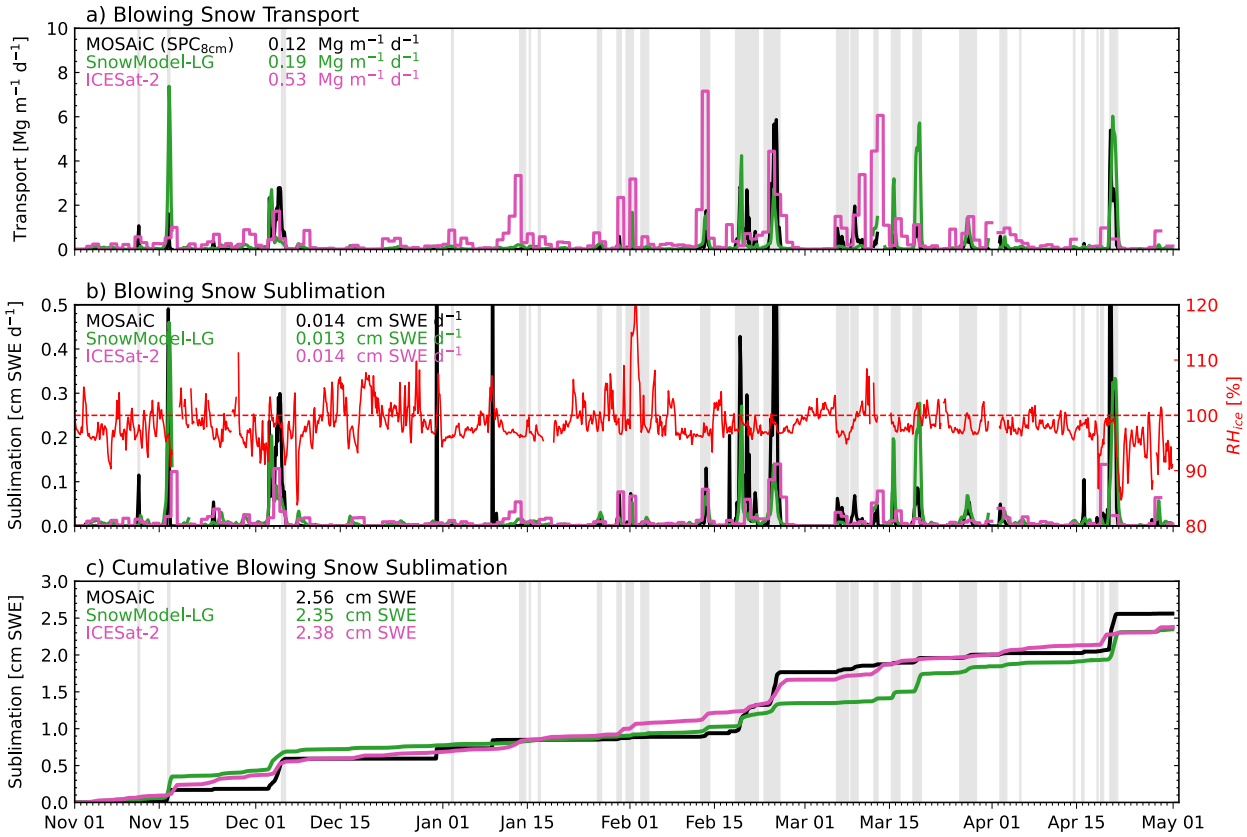

Figure 8. Timeseries of blowing snow transport and sublimation fluxes inferred from MOSAiC observations (black lines), ICESat-2 retrievals (magenta), and predicted by SnowModel-LG (green) between November 2019 and April 2020. **(a)** Blowing snow transport flux (units Mg m^{-1} d^{-1}). The mean value for each dataset is shown in the legend. **(b)** Same as (a) but for the blowing snow sublimation flux (units cm SWE d^{-1}). The relative humidity over ice (RH_{ice}) observed at 10 m during MOSAiC is shown in red. **(c)** Cumulative blowing snow sublimation flux during MOSAiC. The integral of each timeseries is shown in the legend. In November when SPC_{8cm} data were missing in the MOSAiC estimates have been scaled by a constant factor of 44, which is the ratio of 8 cm to 10 m drift densities during December through April periods of blowing snow.

During the majority of blowing snow periods at MOSAiC, the Met City near surface relative humidity over ice (RH_{ice}; red line, Figure 8b) was below saturation and allowed sublimation to

occur. Daily mean sublimation flux values show good agreement between MOSAiC (0.014 cm SWE d^{-1}), SnowModel-LG (0.013 cm SWE d^{-1}), and ICESat-2 (0.014 cm SWE d^{-1}). During the November through April period, we infer a cumulative sublimation of 2.38 cm SWE from ICESat-2 in the region surrounding the MOSAiC drift (Figure 8c). This value is within 10% of both the MOSAiC-based estimate (2.56 cm SWE) and SnowModel-LG prediction (2.35 cm SWE).

Matrosov et al. (2022) and Wagner et al. (2022) conducted a detailed analysis of snowfall and snow accumulation during MOSAiC between the end of October 2019 and the end of April 2020. They report a cumulative snowfall of 7.2 cm SWE based on optical precipitation sensor observations and 10.7 cm SWE based on radar measurements. Furthermore, weekly snow depth measurements from SnowMicroPen retrievals indicated an accumulated snow mass of 3.8 cm SWE. Taken together, these MOSAiC observations suggest a precipitation mass loss of 47-64% near the observatory. Our blowing snow sublimation estimates for the same period are 2.38 cm SWE for ICESat-2 and 2.35 cm SWE for SnowModel-LG, which represent a 22-33% removal of total snowfall and potentially explain a substantial portion of the reported precipitation loss. Static surface (non-blowing snow) sublimation represents an additional precipitation mass loss of 4-5 % (total 0.38 cm SWE) based on SnowModel-LG. Processes causing the remaining precipitation mass loss could include horizontal snow transport, transport into leads, and snow-ice formation (Merkouriadi et al., 2025; Wagner et al., 2022). Liston et al. (2020) found that blowing snow sublimation removed 15% of snowfall when averaged over all Arctic sea ice, but that this fraction could be as large as 30% for the Central Arctic. Our results are broadly consistent with this contribution.

4 Examination of pan-Arctic blowing snow during MOSAiC

Figure 9 shows the spatial variability in Arctic-wide blowing snow occurrence, transport, and sublimation from ICESat-2 and SnowModel-LG between November 2019 and April 2020. For ICESat-2, non-cloudy profiles are averaged to a 100 km EASE grid for each day; clear air profiles are assigned a value of zero for transport and sublimation, while the blowing snow occurrence represents the fraction of non-cloudy profiles in each grid cell that are retrieved as blowing snow. Daily transport and sublimation spatial averages are then computed only for grid cells where less than 70% of ICESat-2 profiles are cloudy. In SnowModel-LG, blowing snow occurrence is defined as the fraction of days with a blowing snow transport flux exceeding 0.02 kg m^{-1} s^{-1} – a threshold selected to match the blowing snow flux inferred from an ICESat-2 blowing snow retrieval with OD = 0.10 at a windspeed of 7 m s^{-1}. This ensures that we only examine SnowModel-LG fluxes that are sufficiently strong for ICESat-2 to detect. Further, we do not consider values from SnowModel-LG grid cells that are labeled as cloudy by ICESat-2. Figure 10 presents the daily averaged timeseries of blowing snow occurrence, transport, and sublimation generated by this procedure.

Both ICESat-2 and SnowModel-LG show a mean blowing snow frequency of 18-28% over the Central Arctic, with the highest values exceeding 20% in the Fram Strait region, consistent with storms entering the Arctic from the midlatitudes (Figure 9a-b). These storms are evident in the pan-Arctic mean blowing snow timeseries as days where both occurrence frequencies peak > 15% (Figure 10a). These days correspond to increases in U_{10m} and decreases in sea-level

pressure both at MOSAiC and predicted by MERRA-2 across all sea ice (Figure S9), suggesting that these storms not only impacted MOSAiC (Rinke et al., 2021) but also the broader Arctic.

While there is overall agreement in the spatial distribution of blowing snow occurrence between ICESat-2 and SnowModel-LG (r = 0.60; Figure 9c), two regions show marked differences. First, ICESat-2 detects blowing snow nearly a quarter of the time in regions north of the Canadian Arctic Archipelago (Figure 9a) while SnowModel-LG maximizes at about a factor of 4 lower (6%). Conversely, SnowModel-LG predicts significant blowing snow (> 20%) off the southeastern coast of Greenland which ICESat-2 does not observe. These two regions will be analyzed in more depth in a subsequent study.

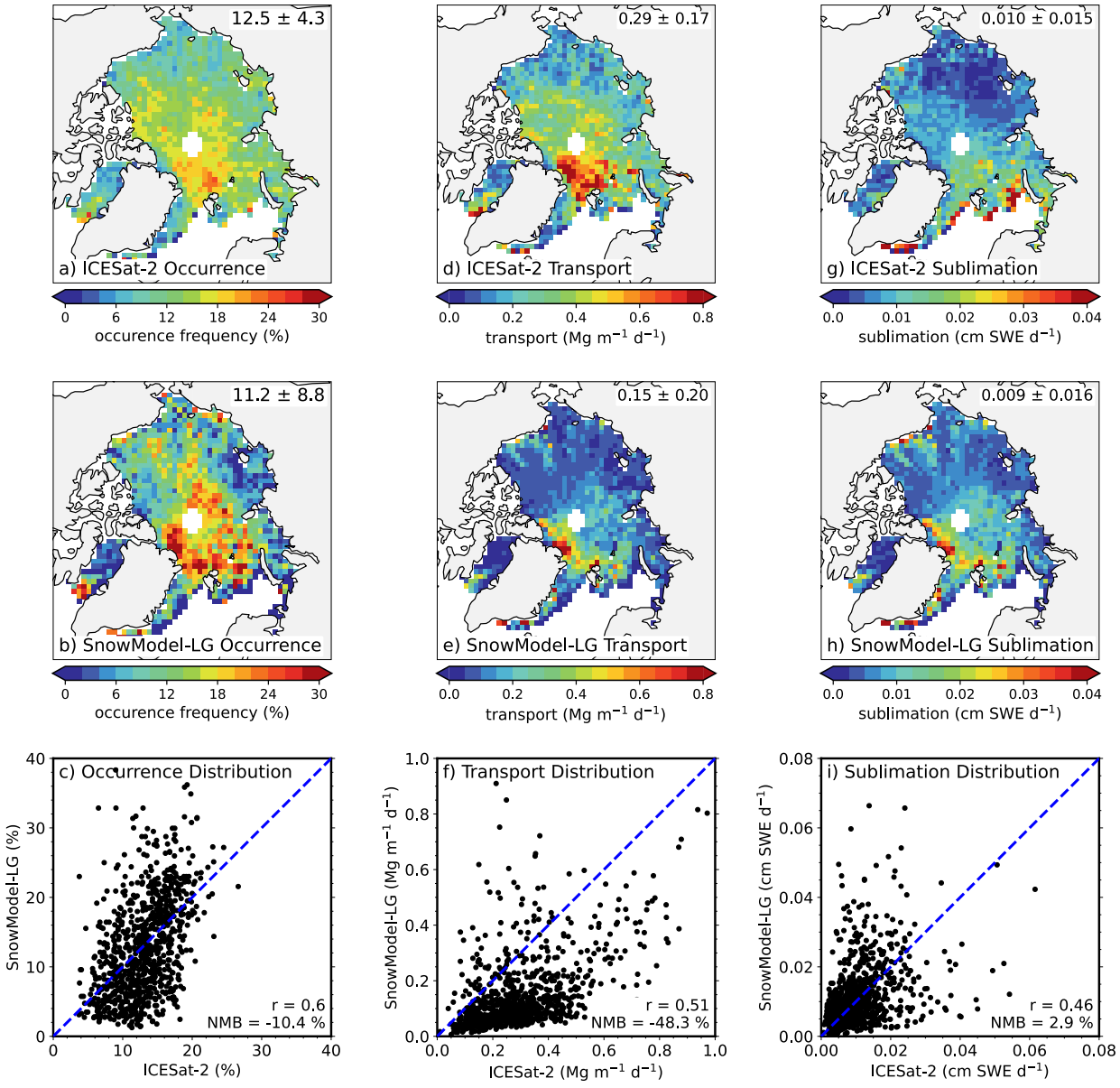

Figure 9. November 2019 through April 2020 mean spatial distribution of blowing snow occurrence **(a,b)** (units %), transport **(d,e)** (units Mg m^{-1} d^{-1}), and sublimation **(g,h)** (units cm SWE d^{-1}) inferred from ICESat-2 and predicted by

SnowModel-LG. The maps are shown on an EASE grid with a resolution of 100 km. The top right of each panel shows the mean and standard deviation. (c) Spatial correlation between ICESat-2 (x-axis) and SnowModel-LG (y-axis) blowing snow frequency from the grid cells shown in panel a. The correlation coefficient and normalized mean bias (NMB) are given in the bottom right. (f) Same as panel c but for blowing snow transport flux. (i) Same as panel c but for blowing snow sublimation.

Transport inferred from ICESat-2 also maximizes in the region of high blowing snow occurrence near the Fram Strait, with values > 0.6 Mg m^{-1} d^{-1} (Figure 9d). SnowModel-LG predicts similar values of transport (> 0.4 Mg m^{-1} d^{-1}) in this region (Figure 9e). The storms driving the occurrence of blowing snow are also seen in the pan-Arctic transport timeseries (Figure 10b), with ICESat-2 and SnowModel-LG displaying peaks > 0.5 Mg m^{-1} d^{-1} on several days in March (Figure 10b).

The mean daily sublimation flux inferred from ICESat-2 and predicted by SnowModel-LG agree to within 15% on average (Figure 9i). The strongest sublimation predicted by SnowModel-LG occurs in March (> 0.04 cm SWE d^{-1}), but ICESat-2 inferred values at these times are a factor of 2 lower at 0.02 cm SWE d^{-1} (Figure 10c). Nevertheless, the ICESat-2 (1.74 cm SWE) and SnowModel-LG (1.79 cm SWE) cumulative blowing snow sublimation amounts averaged across the Arctic for November through April also agree to within 10% (Figure 10d). These totals are broadly consistent with previous SnowModel-LG simulations (1.5 cm SWE; Liston et al., 2020), suggesting ICESat-2 can be used to infer the general temporal evolution of blowing snow sublimation and its role in the snow mass budget on sea ice. Moreover, we find a cumulative snowfall of 10.7 cm SWE over this period predicted by MERRA-2 (Figure S9). Thus ICESat-2 and SnowModel-LG suggest that blowing snow sublimation removes 16-17% of snowfall when averaged across all Arctic sea ice.

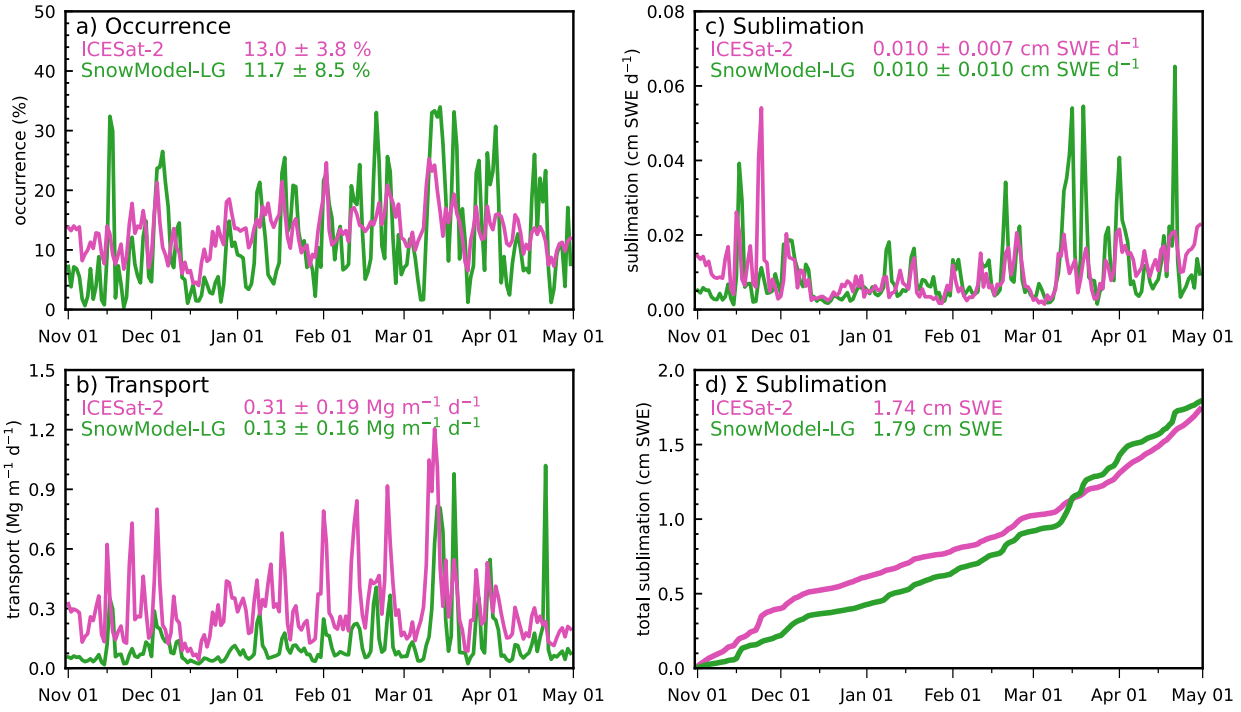

Figure 10. November 2019 through April 2020 daily timeseries of blowing snow occurrence frequency **(a)**, transport flux **(b)**, and sublimation flux **(c)** inferred from ICESat-2 (magenta lines) and predicted by SnowModel-LG (green lines). The daily averaged value is shown in the legend. **(d)** Arctic-wide average accumulative sublimation inferred from ICESat-2 (magenta line) and predicted by SnowModel-LG (green line). The cumulative total is shown in the legend.

ICESat-2 can only detect blowing snow in conditions with clear sky or optically thin clouds. To evaluate the potential bias this introduces, we compare vertically integrated SnowModel-LG blowing snow fluxes for all conditions versus only days with valid ICESat-2 retrievals (Figures S10-S11). SnowModel-LG results from all conditions show the same spatial and temporal patterns as in Figures 9-10 but with values that are 30% larger. These results suggest that the ICESat-2 estimates could be biased low by 30% on average because of this sampling limitation. Scaling the ICESat-2 values to account for this, we find a cumulative blowing snow sublimation flux of 2.26 cm SWE, which equals 21% of MERRA-2 snowfall. SnowModel-LG estimates a cumulative Arctic-wide sublimation under all conditions of 2.27 cm SWE, also resulting in the loss of 21% of snowfall (Figure S11d). Future work will expand this comparison to additional years and seasons to further understand how ICESat-2 samples the underlying variability in blowing snow over Arctic sea ice.

5 Summary and Conclusions

Our analysis presented an optimized ICESat-2 algorithm for detecting blowing snow over Arctic sea ice and demonstrated its ability to capture the occurrence of blowing snow and its properties. This optimization addressed two key issues of retrieving blowing snow when clouds are present. First, we imposed additional quality checks on the retrievals to reclassify clouds misidentified as blowing snow. Second, we introduced a scaling factor which corrects the near-surface backscatter for attenuation by transmissive clouds, thereby allowing retrieval of blowing snow in these instances.

We evaluated the optimized algorithm by examining 612 ICESat-2 overpasses occurring within 100 km of the MOSAiC drifting observatory between November 2019 and April 2020. Both ICESat-2 and the ground-based MOSAiC observations suggest blowing snow occurred 17% of the time during this period. The ability of ICESat-2 to observe the onset, maintenance, and termination of blowing snow was demonstrated for a strong storm on 12-14 February 2020. Across three days, ICESat-2 observed strong blowing snow (ODs > 0.20) coincident with large MOSAiC snow-drift densities ($> 1\times10^{-5}$ kg m^{-3}) and SnowModel-LG blowing snow fluxes ($> 1\times10^{-6}$ Mg m^{-1} s^{-1}). At its peak on 13 February 2020, ICESat-2 observations indicate that the blowing snow event spanned over 1,000 km horizontally and encompassed an area of approximatively 1.5 million km^2, comparable to the geographic extent of Alaska.

We found that ICESat-2 retrieved blowing snow heights (mean 86 m) occurred at or just below temperature inversions identified in coincident radiosonde launches during MOSAiC. Furthermore, both inversion height and retrieved blowing snow height showed a strong dependence on U_{10m}, consistent with increased turbulent mixing at high windspeeds. During coincident periods, blowing snow particle number and mass inferred from ICESat-2 backscatter in the lowest atmospheric bin (0-30 m) showed broad agreement with MOSAiC observations made at 10 m.

We examined all ICESat-2 retrievals within 100 km of MOSAiC and inferred a total of 2.38 cm SWE of blowing snow sublimation, consistent with the total inferred based on the MOSAiC observations (2.56 cm SWE) and SnowModel-LG predictions (2.35 cm SWE). We then used ICESat-2 and SnowModel-LG to examine blowing snow across the entire Arctic during the same six-month period, in general finding good agreement in the spatial structure of blowing snow occurrence. Total pan-Arctic sublimation from ICESat-2 and SnowModel-LG agreed to within 10% (1.74-1.79 cm SWE). These totals represent 16-17% of total pan-Arctic snowfall, consistent with previous studies (e.g., Liston et al., 2020; J. Yang et al., 2010) highlighting the importance of blowing snow sublimation in removing snow from the sea ice surface.

There are a number of factors which could affect the ICESat-2 blowing snow retrievals presented in this work. In cases where falling snow or ice might be mixed with blowing snow, the entire ICESat-2 backscatter signal is attributed to blowing snow, thereby enhancing blowing snow mixing ratios, transport, and sublimation. Further, the temperature and relative humidity profile within blowing snow layers is largely unknown. While we attempted to achieve consistency in assumptions between ICESat-2 and SnowModel-LG, small errors in temperature and humidity can lead to significant changes in derived sublimation. Moreover, blowing snow processes are not included in the MERRA-2 reanalysis and GEOS models and thus their temperature and humidity fields are missing a potentially large source of heat and moisture. Due to the vertical resolution of ICESat-2, the blowing snow algorithm cannot reliably detect blowing snow layers shallower than 30 m. Therefore, the transport and sublimation associated with these layers is not accounted for, potentially biasing the results. With regard to sampling by ICESat-2, no blowing snow can be detected beneath optically thick clouds. These conditions are most often present in and around winter storms which, due to their strong winds, likely generate extensive blowing snow. It is also likely that relative humidities are high beneath these clouds, resulting in suppression of blowing snow sublimation. Conversely, even at these high relative humidities sublimation of small blowing snow particles may still proceed through the Kelvin or curvature effects (X. Yang et al., 2019). To assess the impact of this sampling bias, we examined SnowModel-LG predictions under optically thick cloud conditions and found that ICESat-2 may underestimate sublimation by 30%. However, this approach assumed that SnowModel-LG and MERRA-2 accurately capture the complex sub-cloud storm environment containing blowing snow, falling snow, and nuanced temperature and moisture fields which influence predicted blowing snow sublimation. Future studies should extend the presented analysis approaches beyond MOSAiC to campaigns occurring in additional regions and seasons (e.g., the NASA 2024 Arctic Radiation-Cloud-Aerosol-Surface Interaction EXperiment, ARCSIX) to further evaluate the representativeness of ICESat-2 blowing snow observations and SnowModel-LG predictions.

Arctic sea ice regions are experiencing warming at a rate more than four times the global average (Rantanen et al., 2022). These accelerated changes have been linked to decreasing sea ice extent, thinning sea ice accompanied by a shift to younger ice, and a reduction in the overall snowpack present on sea ice (Meredith et al., 2019; Stroeve et al., 2020; Stroeve & Notz, 2018; Webster et al., 2014). Recent studies have shown that projected continued Arctic warming will also lead to increased precipitation, but that a greater fraction of this precipitation will fall as rain instead of snow (Bintanja, 2018; Bintanja & Andry, 2017; McCrystall et al., 2021). These changes will

likely affect the occurrence and properties of blowing snow, which depend strongly on the amount and characteristics of surface snow. It is therefore more critical than ever to have robust, observational constraints on Arctic blowing snow to accurately capture its characteristics in the present climate and examine potential responses to a changing climate.

Data Availability Statement

The ICESat-2 ATL09 data used in this study can be accessed through the NASA National Snow and Ice Data Center Distributed Active Archive Center (https://doi.org/10.5067/ATLAS/ATL09.006). The MOSAiC data used in this paper were produced on RV Polarstern cruise AWI_PS122_00 as part of the MOSAiC expedition with the tag MOSAiC20192020. Snow-drift density observations from the SPC instruments were contributed by the UKRI Natural Environment Research Council (NERC) and are available through the UK Polar Data Center (https://data.bas.ac.uk/full-record.php?id=GB/NERC/BAS/PDC/01740). The Met City meteorological data were obtained by the University of Colorado and National Oceanic and Atmospheric Administration (NOAA) and can be accessed via the National Science Foundation (NSF) Arctic Data Center (https://arcticdata.io/catalog/view/doi:10.18739/A2PV6B83F). The ceilometer data (https://adc.arm.gov/discovery/#/results/instrument_code::ceil10m/dataLevel::b1) were provided by the Atmospheric Radiation Measurement (ARM) User Facility, a Department of Energy (DOE) Office of Science user facility operated by the Biological and Environmental Research program. The radiosonde data are available via PANGAEA (https://doi.org/10.1594/PANGAEA.943870) and were collected through a partnership between the Alfred Wegner Institute (AWI), the DOE ARM User Facility, and the German Weather Service (DWD).

Acknowledgments

The authors would like to thank the ICESat-2 engineering and science teams for their ongoing efforts to maintain the ATLAS instrument and generate ICESat-2 data products. We also thank all those involved in the collection, processing, and distribution of the MOSAiC data used in this study (Nixdorf et al., 2021). M.D.S. was supported by DOE (DE-SC0021341) and NOAA (NA22OAR4320151; FundRef https://doi/org/10.13039/100018302). M.M.F. was supported by the European Union's Horizon 2020 research and innovation programme under grant agreement No. 101003826 via project CRiceS (Climate Relevant interactions and feedbacks: the key role of sea ice and Snow in the polar and global climate system), the UK Natural Environment Research Council (NERC) (NE/S00257X/1, NE/M005852/1, NE/J021172/1), and the NERC National Capability International grant SURface FluxEs In AnTarctica (SURFEIT) (NE/X009319/1).

Conflict of Interest Statement

The authors have no conflicts of interest to disclose.

6 References

Bintanja, R. (2018). The impact of Arctic warming on increased rainfall. *Scientific Reports*, *8*(1), 16001. https://doi.org/10.1038/s41598-018-34450-3

Bintanja, R., & Andry, O. (2017). Towards a rain-dominated Arctic. *Nature Climate Change*, *7*(4), 263–267. https://doi.org/10.1038/nclimate3240

Brodzik, M. J., & Knowles, K. W. (2002). Chapter 5: EASE-grid: A versatile set of equal-area projections and grids. In M. F. Goodchild (Ed.), Discrete global grids: A web book (pp. 98–113). Santa Barbara, CA: National Center for Geographic Information & Analysis. Retrieved from https://escholarship.org/uc/item/9492q6sm

Chen, W.-N., Chiang, C.-W., & Nee, J.-B. (2002). Lidar ratio and depolarization ratio for cirrus clouds. *Applied Optics*, *41*(30), 6470. https://doi.org/10.1364/AO.41.006470

Choi, S., Theys, N., Salawitch, R. J., Wales, P. A., Joiner, J., Canty, T. P., Chance, K., Suleiman, R. M., Palm, S. P., Cullather, R. I., Darmenov, A. S., Da Silva, A., Kurosu, T. P., Hendrick, F., & Van Roozendael, M. (2018). Link Between Arctic Tropospheric BrO Explosion Observed From Space and Sea-Salt Aerosols From Blowing Snow Investigated Using Ozone Monitoring Instrument BrO Data and GEOS-5 Data Assimilation System. *Journal of Geophysical Research: Atmospheres*, *123*(13), 6954–6983. https://doi.org/10.1029/2017JD026889

Chung, Y.-C., Bélair, S., & Mailhot, J. (2011). Blowing Snow on Arctic Sea Ice: Results from an Improved Sea Ice–Snow–Blowing Snow Coupled System. *Journal of Hydrometeorology*, *12*(4), 678–689. https://doi.org/10.1175/2011JHM1293.1

Cierco, F.-X., Naaim-Bouvet, F., & Bellot, H. (2007). Acoustic sensors for snowdrift measurements: How should they be used for research purposes? *Cold Regions Science and Technology*, *49*(1), 74–87. https://doi.org/10.1016/j.coldregions.2007.01.002

Cox, C. J., Gallagher, M. R., Shupe, M. D., Persson, P. O. G., Solomon, A., Fairall, C. W., Ayers, T., Blomquist, B., Brooks, I. M., Costa, D., Grachev, A., Gottas, D., Hutchings, J. K., Kutchenreiter, M., Leach, J., Morris, S. M., Morris, V., Osborn, J., Pezoa, S., … Uttal, T. (2023). Continuous observations of the surface energy budget and meteorology over the Arctic sea ice during MOSAiC. *Scientific Data*, *10*(1), 519. https://doi.org/10.1038/s41597-023-02415-5

Dai, A. (2008). Temperature and pressure dependence of the rain-snow phase transition over land and ocean. *Geophysical Research Letters*, 35, L12802. https://doi.org/10.1029/2008GL033295

Déry, S. J., & Tremblay, L.-B. (2004). Modeling the Effects of Wind Redistribution on the Snow Mass Budget of Polar Sea Ice*. *Journal of Physical Oceanography*, *34*(1), 258–271. https://doi.org/10.1175/1520-0485(2004)034<0258:MTEOWR>2.0.CO;2

Déry, S. J., & Yau, M. K. (1999). A Bulk Blowing Snow Model. *Boundary-Layer Meteorology*, *93*(2), 237–251. https://doi.org/10.1023/A:1002065615856

Déry, S. J., & Yau, M. K. (2001). Simulation Of Blowing Snow In The Canadian Arctic Using A Double-Moment Model. *Boundary-Layer Meteorology*, *99*(2), 297–316. https://doi.org/10.1023/A:1018965008049

Déry, S. J., & Yau, M. K. (2002). Large-scale mass balance effects of blowing snow and surface sublimation. *Journal of Geophysical Research: Atmospheres*, *107*(D23). https://doi.org/10.1029/2001JD001251

Frey, M. M., Norris, S. J., Brooks, I. M., Anderson, P. S., Nishimura, K., Yang, X., Jones, A. E., Nerentorp Mastromonaco, M. G., Jones, D. H., & Wolff, E. W. (2020). First direct observation of sea salt aerosol production from blowing snow above sea ice. *Atmospheric Chemistry and Physics*, *20*(4), 2549–2578. https://doi.org/10.5194/acp-20-2549-2020

Frey, M., Wagner, D., Kirchgaessner, A., Uttal, T., & Shupe, M. (2023). *Atmospheric snow particle flux in the Central Arctic during MOSAiC 2019-20* (Version 1.0, p. 424 files, 131 MB) [Text/plain,text/csv]. NERC EDS UK Polar Data Centre. https://doi.org/10.5285/7D8E401B-2C75-4EE4-A753-C24B7E91E6E9

Gallée, H., Guyomarc'h, G., & Brun, E. (2001). Impact Of Snow Drift On The Antarctic Ice Sheet Surface Mass Balance: Possible Sensitivity To Snow-Surface Properties. *Boundary-Layer Meteorology*, *99*(1), 1–19. https://doi.org/10.1023/A:1018776422809

Gallée, H., Trouvilliez, A., Agosta, C., Genthon, C., Favier, V., & Naaim-Bouvet, F. (2013). Transport of Snow by the Wind: A Comparison Between Observations in Adélie Land, Antarctica, and Simulations Made with the Regional Climate Model MAR. *Boundary-Layer Meteorology*, *146*(1), 133–147. https://doi.org/10.1007/s10546-012-9764-z

Gelaro, R., McCarty, W., Suárez, M. J., Todling, R., Molod, A., Takacs, L., Randles, C. A., Darmenov, A., Bosilovich, M. G., Reichle, R., Wargan, K., Coy, L., Cullather, R., Draper, C., Akella, S., Buchard, V., Conaty, A., da Silva, A. M., Gu, W., … Zhao, B. (2017). The Modern-Era Retrospective Analysis for Research and Applications, Version 2 (MERRA-2). *Journal of Climate*, *30*(14), 5419–5454. https://doi.org/10.1175/JCLI-D-16-0758.1

Geldsetzer, T., Langlois, A., & Yackel, J. (2009). Dielectric properties of brine-wetted snow on first-year sea ice. *Cold Regions Science and Technology*, *58*(1–2), 47–56. https://doi.org/10.1016/j.coldregions.2009.03.009

Gong, X., Zhang, J., Croft, B., Yang, X., Frey, M. M., Bergner, N., Chang, R. Y.-W., Creamean, J. M., Kuang, C., Martin, R. V., Ranjithkumar, A., Sedlacek, A. J., Uin, J., Willmes, S., Zawadowicz, M. A., Pierce, J. R.,

Shupe, M. D., Schmale, J., & Wang, J. (2023). Arctic warming by abundant fine sea salt aerosols from blowing snow. *Nature Geoscience*, *16*(9), 768–774. https://doi.org/10.1038/s41561-023-01254-8

Herzfeld, U., Hayes, A., Palm, S., Hancock, D., Vaughan, M., & Barbieri, K. (2021). Detection and Height Measurement of Tenuous Clouds and Blowing Snow in ICESat-2 ATLAS Data. *Geophysical Research Letters*, *48*(17), e2021GL093473. https://doi.org/10.1029/2021GL093473

Huang, J., & Jaeglé, L. (2017). Wintertime enhancements of sea salt aerosol in polar regions consistent with a sea ice source from blowing snow. *Atmospheric Chemistry and Physics*, *17*(5), 3699–3712. https://doi.org/10.5194/acp-17-3699-2017

Huang, J., Jaeglé, L., Chen, Q., Alexander, B., Sherwen, T., Evans, M. J., Theys, N., & Choi, S. (2020). Evaluating the impact of blowing-snow sea salt aerosol on springtime BrO and O₃ in the Arctic. *Atmospheric Chemistry and Physics*, *20*(12), 7335–7358. https://doi.org/10.5194/acp-20-7335-2020

Josset, D., Pelon, J., Garnier, A., Hu, Y., Vaughan, M., Zhai, P., Kuehn, R., & Lucker, P. (2012). Cirrus optical depth and lidar ratio retrieval from combined CALIPSO-CloudSat observations using ocean surface echo. *Journal of Geophysical Research: Atmospheres*, *117*(D5), 2011JD016959. https://doi.org/10.1029/2011JD016959

Jozef, G. C., Cassano, J. J., Dahlke, S., Dice, M., Cox, C. J., & De Boer, G. (2024). An overview of the vertical structure of the atmospheric boundary layer in the central Arctic during MOSAiC. *Atmospheric Chemistry and Physics*, *24*(2), 1429–1450. https://doi.org/10.5194/acp-24-1429-2024

Jozef, G. C., Klingel, R., Cassano, J. J., Maronga, B., De Boer, G., Dahlke, S., & Cox, C. J. (2023). Derivation and compilation of lower-atmospheric properties relating to temperature, wind, stability, moisture, and surface radiation budget over the central Arctic sea ice during MOSAiC. *Earth System Science Data*, *15*(11), 4983–4995. https://doi.org/10.5194/essd-15-4983-2023

King, J. C., Anderson, P. S., Vaughan, D. G., Mann, G. W., Mobbs, S. D., & Vosper, S. B. (2004). Wind-borne redistribution of snow across an Antarctic ice rise. *Journal of Geophysical Research: Atmospheres*, *109*(D11), 2003JD004361. https://doi.org/10.1029/2003JD004361

Knust, R. (2017). Polar Research and Supply Vessel POLARSTERN Operated by the Alfred-Wegener-Institute. *Journal of Large-Scale Research Facilities JLSRF*, *3*, A119. https://doi.org/10.17815/jlsrf-3-163

Krnavek, L., Simpson, W. R., Carlson, D., Domine, F., Douglas, T. A., & Sturm, M. (2012). The chemical composition of surface snow in the Arctic: Examining marine, terrestrial, and atmospheric influences. *Atmospheric Environment*, *50*, 349–359. https://doi.org/10.1016/j.atmosenv.2011.11.033

Lecomte, O., Fichefet, T., Flocco, D., Schroeder, D., & Vancoppenolle, M. (2015). Interactions between wind-blown snow redistribution and melt ponds in a coupled ocean–sea ice model. *Ocean Modelling*, *87*, 67–80. https://doi.org/10.1016/j.ocemod.2014.12.003

Lenaerts, J. T. M., Van Den Broeke, M. R., Déry, S. J., König-Langlo, G., Ettema, J., & Munneke, P. K. (2010). Modelling snowdrift sublimation on an Antarctic ice shelf. *The Cryosphere*, *4*(2), 179–190. https://doi.org/10.5194/tc-4-179-2010

Lenaerts, J. T. M., Van Den Broeke, M. R., Van Angelen, J. H., Van Meijgaard, E., & Déry, S. J. (2012). Drifting snow climate of the Greenland ice sheet: A study with a regional climate model. *The Cryosphere*, *6*(4), 891–899. https://doi.org/10.5194/tc-6-891-2012

Lesins, G., Bourdages, L., Duck, T. J., Drummond, J. R., Eloranta, E. W., & Walden, V. P. (2009). Large surface radiative forcing from topographic blowing snow residuals measured in the High Arctic at Eureka. *Atmospheric Chemistry and Physics*, *9*(6), 1847–1862. https://doi.org/10.5194/acp-9-1847-2009

Li, L., & Pomeroy, J. W. (1997). Probability of occurrence of blowing snow. *Journal of Geophysical Research: Atmospheres*, *102*(D18), 21955–21964. https://doi.org/10.1029/97JD01522

Liston, G. E., Haehnel, R. B., Sturm, M., Hiemstra, C. A., Berezovskaya, S., & Tabler, R. D. (2007). Simulating complex snow distributions in windy environments using SnowTran-3D. *Journal of Glaciology*, *53*(181), 241–256. https://doi.org/10.3189/172756507782202865

Liston, G. E., Itkin, P., Stroeve, J., Tschudi, M., Stewart, J. S., Pedersen, S. H., Reinking, A. K., & Elder, K. (2020). A Lagrangian Snow-Evolution System for Sea-Ice Applications (SnowModel-LG): Part I—Model Description. *Journal of Geophysical Research: Oceans*, *125*(10). https://doi.org/10.1029/2019JC015913

Liston, G. E., Polashenski, C., Rösel, A., Itkin, P., King, J., Merkouriadi, I., & Haapala, J. (2018). A Distributed Snow-Evolution Model for Sea-Ice Applications (SnowModel). *Journal of Geophysical Research: Oceans*, *123*(5), 3786–3810. https://doi.org/10.1002/2017JC013706

Liston, G. E., & Sturm, M. (1998). A snow-transport model for complex terrain. *Journal of Glaciology*, *44*(148), 498–516. https://doi.org/10.3189/S0022143000002021

Liston, G. E., & Sturm, M. (2004). The role of winter sublimation in the Arctic moisture budget. *Hydrology Research*, *35*(4–5), 325–334. https://doi.org/10.2166/nh.2004.0024

Liston, G. E., & Elder, K. (2006). A meteorological distribution system for high-resolution terrestrial modeling (MicroMet). *Journal of Hydrometeorology*, 7(2), 217–234. https://doi.org/10.1175/JHM486.1

Lucchesi, R. (2015). File Specification for GEOS-5 FP-IT. *GMAO Office Note No. 2 (Version 1.3)*, 60 pp, available from http://gmao.gsfc.nasa.gov/pubs/office_notes.

Mann, G. W., Anderson, P. S., & Mobbs, S. D. (2000). Profile measurements of blowing snow at Halley, Antarctica. *Journal of Geophysical Research: Atmospheres*, *105*(D19), 24491–24508. https://doi.org/10.1029/2000JD900247

Marelle, L., Thomas, J. L., Ahmed, S., Tuite, K., Stutz, J., Dommergue, A., Simpson, W. R., Frey, M. M., & Baladima, F. (2021). Implementation and Impacts of Surface and Blowing Snow Sources of Arctic Bromine Activation Within WRF-Chem 4.1.1. *Journal of Advances in Modeling Earth Systems*, *13*(8), e2020MS002391. https://doi.org/10.1029/2020MS002391

Markus, T., Neumann, T., Martino, A., Abdalati, W., Brunt, K., Csatho, B., Farrell, S., Fricker, H., Gardner, A., Harding, D., Jasinski, M., Kwok, R., Magruder, L., Lubin, D., Luthcke, S., Morison, J., Nelson, R., Neuenschwander, A., Palm, S., … Zwally, J. (2017). The Ice, Cloud, and land Elevation Satellite-2 (ICESat-2): Science requirements, concept, and implementation. *Remote Sensing of Environment*, *190*, 260–273. https://doi.org/10.1016/j.rse.2016.12.029

Matrosov, S. Y., Shupe, M. D., & Uttal, T. (2022). High temporal resolution estimates of Arctic snowfall rates emphasizing gauge and radar-based retrievals from the MOSAiC expedition. *Elementa: Science of the Anthropocene*, *10*(1), 00101. https://doi.org/10.1525/elementa.2021.00101

McCrystall, M. R., Stroeve, J., Serreze, M., Forbes, B. C., & Screen, J. A. (2021). New climate models reveal faster and larger increases in Arctic precipitation than previously projected. *Nature Communications*, *12*(1), 6765. https://doi.org/10.1038/s41467-021-27031-y

Merkouriadi I., Jutila A., Liston G. E., Preußer A., & Webster M. A. (2025). Investigating snow sinks on level sea ice: A case study in the western Arctic. *Journal of Glaciology*, 71, e66, 1–13. https://doi.org/10.1017/jog.2025.34

Naaim-Bouvet, F., Bellot, H., & Naaim, M. (2010). Back analysis of drifting-snow measurements over an instrumented mountainous site. *Annals of Glaciology*, *51*(54), 207–217. https://doi.org/10.3189/172756410791386661

Neumann, T. A., Martino, A. J., Markus, T., Bae, S., Bock, M. R., Brenner, A. C., Brunt, K. M., Cavanaugh, J., Fernandes, S. T., Hancock, D. W., Harbeck, K., Lee, J., Kurtz, N. T., Luers, P. J., Luthcke, S. B., Magruder, L., Pennington, T. A., Ramos-Izquierdo, L., Rebold, T., … Thomas, T. C. (2019). The Ice, Cloud, and Land Elevation Satellite – 2 mission: A global geolocated photon product derived from the Advanced Topographic Laser Altimeter System. *Remote Sensing of Environment*, *233*, 111325. https://doi.org/10.1016/j.rse.2019.111325

Nicolaus, M., Perovich, D. K., Spreen, G., Granskog, M. A., Von Albedyll, L., Angelopoulos, M., Anhaus, P., Arndt, S., Belter, H. J., Bessonov, V., Birnbaum, G., Brauchle, J., Calmer, R., Cardellach, E., Cheng, B., Clemens-Sewall, D., Dadic, R., Damm, E., De Boer, G., … Wendisch, M. (2022). Overview of the MOSAiC expedition: Snow and sea ice. *Elem Sci Anth*, *10*(1), 000046. https://doi.org/10.1525/elementa.2021.000046

Nishimura, K., & Nemoto, M. (2005). Blowing snow at Mizuho station, Antarctica. *Philosophical Transactions of the Royal Society A: Mathematical, Physical and Engineering Sciences*, *363*(1832), 1647–1662. https://doi.org/10.1098/rsta.2005.1599

Nishimura, K., Yokoyama, C., Ito, Y., Nemoto, M., Naaim-Bouvet, F., Bellot, H., & Fujita, K. (2014). Snow particle speeds in drifting snow. *Journal of Geophysical Research: Atmospheres*, *119*(16), 9901–9913. https://doi.org/10.1002/2014JD021686

Nixdorf, U., Dethloff, K., Rex, M., Shupe, M., Sommerfeld, A., Perovich, D. K., Nicolaus, M., Heuzé, C., Rabe, B., Loose, B., Damm, E., Gradinger, R., Fong, A., Maslowski, W., Rinke, A., Kwok, R., Spreen, G., Wendisch, M., Herber, A., … Boetius, A. (2021). *MOSAiC Extended Acknowledgement*. Zenodo. https://doi.org/10.5281/ZENODO.5179738

Palm, S. P., Kayetha, V., & Yang, Y. (2018). Toward a Satellite-Derived Climatology of Blowing Snow Over Antarctica. *Journal of Geophysical Research: Atmospheres*, *123*(18). https://doi.org/10.1029/2018JD028632

Palm, S. P., Kayetha, V., Yang, Y., & Pauly, R. (2017). Blowing snow sublimation and transport over Antarctica from 11 years of CALIPSO observations. *The Cryosphere*, *11*(6), 2555–2569. https://doi.org/10.5194/tc-11-2555-2017

Palm, S. P., Y. Yang, U. C. Herzfeld, D. Hancock, K. A. Barbieri, J. Wimert, & Team, T. Ices.-2 S. (2023). *ATLAS/ICESat-2 L3A Calibrated Backscatter Profiles and Atmospheric Layer Characteristics, Version 6* [Dataset]. NASA National Snow and Ice Data Center Distributed Active Archive Center. https://doi.org/10.5067/ATLAS/ATL09.006

Palm, S. P., Yang, Y., Herzfeld, U., Hancock, D., Hayes, A., Selmer, P., Hart, W., & Hlavka, D. (2021). ICESat-2 Atmospheric Channel Description, Data Processing and First Results. *Earth and Space Science*, *8*(8), e2020EA001470. https://doi.org/10.1029/2020EA001470

Palm, S. P., Yang, Y., Kayetha, V., & Nicolas, J. P. (2018). Insight into the Thermodynamic Structure of Blowing-Snow Layers in Antarctica from Dropsonde and CALIPSO Measurements. *Journal of Applied Meteorology and Climatology*, *57*(12), 2733–2748. https://doi.org/10.1175/JAMC-D-18-0082.1

Palm, S. P., Yang, Y., Spinhirne, J. D., & Marshak, A. (2011). Satellite remote sensing of blowing snow properties over Antarctica. *Journal of Geophysical Research*, *116*(D16), D16123. https://doi.org/10.1029/2011JD015828

Palm, S., Yang, Y., Hertzfeld, U., & Hancock, D. (2022). *Ice, Cloud, and Land Elevation Satellite (ICESat-2) Project Algorithm Theoretical Basis Document for the Atmosphere, Part I: Level 2 and 3 Data Products, version 6*. https://doi.org/10.5067/H975R4YYVIT6

Perovich, D. K., & Richter-Menge, J. A. (1994). Surface characteristics of lead ice. *Journal of Geophysical Research*, *99*(C8), 16341. https://doi.org/10.1029/94JC01194

Peterson, P. K., Hartwig, M., May, N. W., Schwartz, E., Rigor, I., Ermold, W., Steele, M., Morison, J. H., Nghiem, S. V., & Pratt, K. A. (2019). Snowpack measurements suggest role for multi-year sea ice regions in Arctic atmospheric bromine and chlorine chemistry. *Elementa: Science of the Anthropocene*, *7*, 14. https://doi.org/10.1525/elementa.352

Pomeroy, J. W., Marsh, P., & Gray, D. M. (1997). Application of a distributed blowing snow model to the Arctic. *Hydrological Processes*, *11*(11), 1451–1464. https://doi.org/10.1002/(SICI)1099-1085(199709)11:11<1451::AID-HYP449>3.0.CO;2-Q

Rabe, B., Heuzé, C., Regnery, J., Aksenov, Y., Allerholt, J., Athanase, M., Bai, Y., Basque, C., Bauch, D., Baumann, T. M., Chen, D., Cole, S. T., Craw, L., Davies, A., Damm, E., Dethloff, K., Divine, D. V., Doglioni, F., Ebert, F., … Zhu, J. (2022). Overview of the MOSAiC expedition: Physical oceanography. *Elem Sci Anth*, *10*(1), 00062. https://doi.org/10.1525/elementa.2021.00062

Ranjithkumar, A., Duncan, E., Yang, X., Partridge, D., Lachlan-Cope, T., Gong, X., Nishimura, K., & Frey, M. M. (2025). Direct observation of Arctic Sea salt aerosol production from blowing snow and modelling over a changing sea ice environment, *Elementa: Science of the Anthropocene*, 13, 1. https://doi.org/10.1525/elementa.2024.00006

Rantanen, M., Karpechko, A. Yu., Lipponen, A., Nordling, K., Hyvärinen, O., Ruosteenoja, K., Vihma, T., & Laaksonen, A. (2022). The Arctic has warmed nearly four times faster than the globe since 1979. *Communications Earth & Environment*, *3*(1), 168. https://doi.org/10.1038/s43247-022-00498-3

Rhodes, R. H., Yang, X., Wolff, E. W., McConnell, J. R., & Frey, M. M. (2017). Sea ice as a source of sea salt aerosol to Greenland ice cores: A model-based study. *Atmospheric Chemistry and Physics*, *17*(15), 9417–9433. https://doi.org/10.5194/acp-17-9417-2017

Rinke, A., Cassano, J. J., Cassano, E. N., Jaiser, R., & Handorf, D. (2021). Meteorological conditions during the MOSAiC expedition. *Elementa: Science of the Anthropocene*, *9*(1), 00023. https://doi.org/10.1525/elementa.2021.00023

Schmidt, R. A. (1982). Vertical profiles of wind speed, snow concentration, and humidity in blowing snow. *Boundary-Layer Meteorology*, *23*(2), 223–246. https://doi.org/10.1007/BF00123299

Shupe, M. D., Rex, M., Blomquist, B., Persson, P. O. G., Schmale, J., Uttal, T., Althausen, D., Angot, H., Archer, S., Bariteau, L., Beck, I., Bilberry, J., Bucci, S., Buck, C., Boyer, M., Brasseur, Z., Brooks, I. M., Calmer, R., Cassano, J., … Yue, F. (2022). Overview of the MOSAiC expedition: Atmosphere. *Elem Sci Anth*, *10*(1), 00060. https://doi.org/10.1525/elementa.2021.00060

Shupe, M. D., Walden, V. P., Eloranta, E., Uttal, T., Campbell, J. R., Starkweather, S. M., & Shiobara, M. (2011). Clouds at Arctic Atmospheric Observatories. Part I: Occurrence and Macrophysical Properties. *Journal of Applied Meteorology and Climatology*, *50*(3), 626–644. https://doi.org/10.1175/2010JAMC2467.1

Simpson, W. R., von Glasow, R., Riedel, K., Anderson, P., Ariya, P., Bottenheim, J., Burrows, J., Carpenter, L. J., Frieß, U., Goodsite, M. E., Heard, D., Hutterli, M., Jacobi, H.-W., Kaleschke, L., Neff, B., Plane, J., Platt,

U., Richter, A., Roscoe, H., … Wolff, E. (2007). Halogens and their role in polar boundary-layer ozone depletion. *Atmospheric Chemistry and Physics*, *7*(16), 4375–4418. https://doi.org/10.5194/acp-7-4375-2007

Sterk, H. A. M., Steeneveld, G. J., & Holtslag, A. A. M. (2013). The role of snow-surface coupling, radiation, and turbulent mixing in modeling a stable boundary layer over Arctic sea ice. *Journal of Geophysical Research: Atmospheres*, *118*(3), 1199–1217. https://doi.org/10.1002/jgrd.50158

Stroeve, J., Liston, G. E., Buzzard, S., Zhou, L., Mallett, R., Barrett, A., Tschudi, M., Tsamados, M., Itkin, P., & Stewart, J. S. (2020). A Lagrangian Snow Evolution System for Sea Ice Applications (SnowModel-LG): Part II—Analyses. *Journal of Geophysical Research: Oceans*, *125*(10), e2019JC015900. https://doi.org/10.1029/2019JC015900

Stroeve, J., & Notz, D. (2018). Changing state of Arctic sea ice across all seasons. *Environmental Research Letters*, *13*(10), 103001. https://doi.org/10.1088/1748-9326/aade56

Swanson, W. F., Holmes, C. D., Simpson, W. R., Confer, K., Marelle, L., Thomas, J. L., Jaeglé, L., Alexander, B., Zhai, S., Chen, Q., Wang, X., & Sherwen, T. (2022). Comparison of model and ground observations finds snowpack and blowing snow aerosols both contribute to Arctic tropospheric reactive bromine. *Atmospheric Chemistry and Physics*, *22*(22), 14467–14488. https://doi.org/10.5194/acp-22-14467-2022

Tschudi, M. A., Meier, W. N., & Stewart, J. S. (2020). An enhancement to sea ice motion and age products at the National Snow and Ice Data Center (NSIDC). *The Cryosphere*, *14*(5), 1519–1536. https://doi.org/10.5194/tc-14-1519-2020

Tschudi, M. & Univ Of CO. (2019). *Polar Pathfinder Daily 25 km EASE-Grid Sea Ice Motion Vectors* [Dataset]. NASA National Snow and Ice Data Center Distributed Active Archive Center. https://doi.org/10.5067/INAWUWO7QH7B

Wagner, D. N., Shupe, M. D., Cox, C., Persson, O. G., Uttal, T., Frey, M. M., Kirchgaessner, A., Schneebeli, M., Jaggi, M., Macfarlane, A. R., Itkin, P., Arndt, S., Hendricks, S., Krampe, D., Nicolaus, M., Ricker, R., Regnery, J., Kolabutin, N., Shimanshuck, E., … Lehning, M. (2022). Snowfall and snow accumulation during the MOSAiC winter and spring seasons. *The Cryosphere*, *16*(6), 2373–2402. https://doi.org/10.5194/tc-16-2373-2022

Wales, P. A., Keller, C. A., Knowland, K. E., Pawson, S., Choi, S., Hendrick, F., Van Roozendael, M., Salawitch, R. J., Sulieman, R., & Swanson, W. F. (2023). Application of Satellite-Based Detections of Arctic Bromine Explosion Events Within GEOS-Chem. *Journal of Advances in Modeling Earth Systems*, *15*(8), e2022MS003465. https://doi.org/10.1029/2022MS003465

Webster, M. A., Rigor, I. G., Nghiem, S. V., Kurtz, N. T., Farrell, S. L., Perovich, D. K., & Sturm, M. (2014). Interdecadal changes in snow depth on Arctic sea ice. *Journal of Geophysical Research: Oceans*, *119*(8), 5395–5406. https://doi.org/10.1002/2014JC009985

Winker, D. M., Vaughan, M. A., Omar, A., Hu, Y., Powell, K. A., Liu, Z., Hunt, W. H., & Young, S. A. (2009). Overview of the CALIPSO Mission and CALIOP Data Processing Algorithms. *Journal of Atmospheric and Oceanic Technology*, *26*(11), 2310–2323. https://doi.org/10.1175/2009JTECHA1281.1

Yang, J., Yau, M. K., Fang, X., & Pomeroy, J. W. (2010). A triple-moment blowing snow-atmospheric model and its application in computing the seasonal wintertime snow mass budget. *Hydrology and Earth System Sciences*, *14*(6), 1063–1079. https://doi.org/10.5194/hess-14-1063-2010

Yang, X., Frey, M. M., Rhodes, R. H., Norris, S. J., Brooks, I. M., Anderson, P. S., Nishimura, K., Jones, A. E., & Wolff, E. W. (2019). Sea salt aerosol production via sublimating wind-blown saline snow particles over sea ice: Parameterizations and relevant microphysical mechanisms. *Atmospheric Chemistry and Physics*, *19*(13), 8407–8424. https://doi.org/10.5194/acp-19-8407-2019

Yang, X., Pyle, J. A., Cox, R. A., Theys, N., & Van Roozendael, M. (2010). Snow-sourced bromine and its implications for polar tropospheric ozone, Atmospheric Chemistry and Physics, 10, 7763–7773, https://doi.org/10.5194/acp-10-7763-2010.

Yang, X., Pyle, J. A., & Cox, R. A. (2008). Sea salt aerosol production and bromine release: Role of snow on sea ice. *Geophysical Research Letters*, *35*(16), L16815. https://doi.org/10.1029/2008GL034536

Yang, Y., Palm, S. P., Marshak, A., Wu, D. L., Yu, H., & Fu, Q. (2014). First satellite-detected perturbations of outgoing longwave radiation associated with blowing snow events over Antarctica. *Geophysical Research Letters*, *41*(2), 730–735. https://doi.org/10.1002/2013GL058932

Zhang, D., Vogelmann, A., Kollias, P., Luke, E., Yang, F., Lubin, D., & Wang, Z. (2019). Comparison of Antarctic and Arctic Single-Layer Stratiform Mixed-Phase Cloud Properties Using Ground-Based Remote Sensing Measurements. *Journal of Geophysical Research: Atmospheres*, *124*(17–18), 10186–10204. https://doi.org/10.1029/2019JD030673